AzTEC half square degree survey of the SHADES fields – II. Identifications, redshifts and evidence for large-scale structure

Michał J. Michałowski,[1]* J. S. Dunlop,[1] R. J. Ivison,[1,2] M. Cirasuolo,[1,2] K. I. Caputi,[1,3] I. Aretxaga,[4] V. Arumugam,[1] J. E. Austermann,[5] E. L. Chapin,[6,7] S. C. Chapman,[8] K. E. K. Coppin,[9] E. Egami,[10] D. H. Hughes,[4] E. Ibar,[2] A. M. J. Mortier,[1,11] A. M. Schael,[1,12] K. S. Scott,[13] I. Smail,[14] T. A. Targett,[1] J. Wagg,[15] G. W. Wilson,[16] L. Xu[10] and M. Yun[16]

[1]*SUPA†, Institute for Astronomy, University of Edinburgh, Royal Observatory, Edinburgh EH9 3HJ*
[2]*UK Astronomy Technology Centre, Royal Observatory, Edinburgh EH9 3HJ*
[3]*Kapteyn Astronomical Institute, University of Groningen, PO Box 800, 9700 AV Groningen, the Netherlands*
[4]*Instituto Nacional de Astrofísica, Óptica y Electrónica (INAOE), Aptdo. Postal 51 y 216, 72000 Puebla, Puebla, Mexico*
[5]*Center for Astrophysics and Space Astronomy, University of Colorado, Boulder, CO 80309, USA*
[6]*Department of Physics & Astronomy, University of British Columbia, 6224 Agricultural Road, Vancouver, BC V6T 1Z1, Canada*
[7]*XMM SOC, ESAC, Apartado 78, 28691 Villanueva de la Cañada, Madrid, Spain*
[8]*Institute of Astronomy, University of Cambridge, Madingley Road, Cambridge CB3 0HA*
[9]*Department of Physics, McGill University, 3600 Rue University, Montreal, QC H3A 2T8, Canada*
[10]*Steward Observatory, University of Arizona, 933 North Cherry Avenue, Tucson, AZ 85721, USA*
[11]*Astrophysics Group, Imperial College London, Blackett Laboratory, Prince Consort Road, London SW7 2AZ*
[12]*Max Planck Institute for Extraterrestrial Physics, 85748 Garching bei München, Germany*
[13]*North American ALMA Science Center, National Radio Astronomy Observatory, Charlottesville, VA 22903, USA*
[14]*Institute for Computational Cosmology, Durham University, South Road, Durham DH1 3LE*
[15]*European Southern Observatory, Casilla 19001, Santiago, Chile*
[16]*Department of Astronomy, University of Massachusetts, Amherst, MA 01003, USA*

ABSTRACT

The Astronomical Thermal Emission Camera (AzTEC) 1.1 mm survey of the two SCUBA HAlf Degree Extragalactic Survey (SHADES) fields is the largest ($0.7\,\mathrm{deg}^2$) blank-field millimetre-wavelength (mm-wavelength) survey undertaken to date at a resolution of $\simeq 18$ arcsec and a depth of $\simeq 1$ mJy. We have used the deep optical to radio multiwavelength data in the SHADES Lockman Hole East and SXDF/UDS fields to obtain galaxy identifications for $\simeq 64$ per cent ($\simeq 80$ per cent including tentative identifications) of the 148 AzTEC-SHADES 1.1 mm sources reported by Austermann et al., exploiting deep radio and $24\,\mu m$ data complemented by methods based on $8\,\mu m$ flux density and red optical–infrared ($i - K$) colour. This unusually high identification rate can be attributed to the relatively bright mm-wavelength flux density threshold, combined with the relatively deep supporting multi-frequency data now available in these two well-studied fields. We have further exploited the optical–mid-infrared–radio data to derive an $\simeq 60$ per cent ($\simeq 75$ per cent including tentative identifications) complete redshift distribution for the AzTEC-SHADES sources, yielding a median redshift of $z \simeq 2.2$, with a high-redshift tail extending to at least $z \simeq 4$. Despite the larger area probed by the AzTEC survey relative to the original SCUBA-SHADES imaging, the redshift distribution of the AzTEC sources is consistent with that displayed by the SCUBA sources, and reinforces tentative evidence that the redshift distribution of mm/submm sources in the Lockman Hole field is significantly different from that found in the SXDF/UDS field.

*E-mail: mm@roe.ac.uk
†Scottish Universities Physics Alliance.

Comparison with simulated surveys of similar scale extracted from semi-analytic models based on the Millennium simulation indicates that this is as expected if the mm/submm sources are massive ($M > 10^{11}\,\mathrm{M_\odot}$) star-forming galaxies tracing large-scale structures over scales of 10–20 Mpc. This confirms the importance of surveys covering several $\deg^2$ (as now underway with SCUBA2) to obtain representative samples of bright (sub)mm-selected galaxies. This work provides a foundation for the further exploitation of the *Spitzer* and *Herschel* data in the SHADES fields in the study of the stellar masses and specific star formation rates of the most active star-forming galaxies in cosmic history.

Key words: galaxies: distances and redshifts – galaxies: evolution – galaxies: high-redshift – galaxies: stellar content – cosmology: miscellaneous – submillimetre: galaxies.

1 INTRODUCTION

The objects uncovered by high Galactic latitude surveys at (sub)millimetre [sub(mm)] wavelengths (generally termed 'submm galaxies', hereafter SMGs) are now understood to be distant ($z \simeq 2$–3) and massive ($\simeq 10^{11}\,\mathrm{M_\odot}$) star-forming galaxies (Aretxaga et al. 2003, 2007; Dannerbauer et al. 2004; Smail et al. 2004; Swinbank et al. 2004, 2006; Takagi, Hanami & Arimoto 2004; Borys et al. 2005; Chapman et al. 2005; Greve et al. 2005; Tacconi et al. 2006, 2008; Eales et al. 2009; Amblard et al. 2010; Dunlop et al. 2010; Engel et al. 2010; Michałowski, Hjorth & Watson 2010a; Michałowski, Watson & Hjorth 2010b; Santini et al. 2010; Hainline et al. 2011; Hayward, Kereš, Jonsson et al. 2011; Targett et al. 2011, 2012; Wardlow et al. 2011; Béthermin et al. 2012; Bussmann et al. 2012; Michałowski et al. 2012; Shimizu, Yoshida & Okamoto 2012; Yun et al. 2012). However, the role of these spectacular objects in the cosmic history of galaxy/star formation has yet to be properly established.

The majority of the submm surveys undertaken with the Submillimetre Common-User Bolometer Array (SCUBA; Holland et al. 1999) on the James Clerk Maxwell Telescope (JCMT) covered small ($<0.03\,\deg^2$) fields due to sensitivity and time-constraints (Smail, Ivison & Blain 1997; Barger et al. 1998; Hughes et al. 1998; Barger, Cowie & Sanders 1999; Barger, Cowie & Richards 2000; Barger et al. 2001, 2002; Chapman et al. 2001, 2003; Scott et al. 2002; Webb et al. 2003; Wang, Cowie & Barger 2004; Coppin et al. 2005; Pope et al. 2006). Only two submm surveys completed to date cover a significant fraction of a degree: the SCUBA HAlf Degree Extragalactic Survey (SHADES; $0.2\,\deg^2$; Mortier et al. 2005; Coppin et al. 2006) undertaken at the JCMT and the $870\,\mu\mathrm{m}$ survey of the *Extended Chandra Deep Field*-South (ECDF-S) ($0.25\,\deg^2$; Weiß et al. 2009) performed with the Large APEX BOlometer CAmera (LABOCA; Siringo et al. 2009) on the Atacama Pathfinder EXperiment (APEX).

At slightly longer wavelengths (1.1–1.2 mm) surveys with the Max-Planck Millimeter Bolometer (MAMBO) array on the IRAM 30-m telescope, and with the Astronomical Thermal Emission Camera (AzTEC; Wilson et al. 2008) on the JCMT and Atacama Submillimeter Telescope Experiment (ASTE; Ezawa et al. 2004, 2008) have generally covered areas of $<0.25\,\deg^2$ (Greve et al. 2004, 2008; Bertoldi et al. 2007; Perera et al. 2008; Scott et al. 2008, 2010; Austermann et al. 2009; Hatsukade et al. 2011; Lindner et al. 2011). The notable exceptions are the MAMBO survey of the (possibly lensed) field of the cluster Abell 2125 totalling $0.44\,\deg^2$ (Wagg et al. 2009), and the AzTEC/ASTE survey of the COSMOS field with an $\simeq 34$ arcsec beam covering $0.72\,\deg^2$ (Aretxaga et al. 2011).

There are a number of reasons why it is necessary to analyse SMG properties in fields with significant sizes (of the order of a $\deg^2$ or more). Smaller fields miss the rare members of the SMG population, that is, both low- and high-redshift parts of the distribution as well as the bright end of the luminosity function. Moreover, the clustering properties and large-scale structures traced by SMGs can only be studied in fields larger than these structures. Finally, significant field-to-field variation (cosmic variance) advocates the need of observing multiple well-separated fields.

Here we analyse the properties of the galaxies detected in the largest very deep (rms 0.9–1.7 mJy beam^{-1}) blank-field mm survey of the Lockman Hole East and the *Subaru/XMM–Newton Deep Field* (SXDF) [aka the UKIDSS Ultra Deep Survey (UDS) field] conducted with the AzTEC mounted on the JCMT [beam size of 18 arcsec full width at half-maximum (FWHM)] which covers a total area of $0.7\,\deg^2$ (Austermann et al. 2010). At present, the only substantially larger mm-wavelength survey is the $87\,\deg^2$ survey programme undertaken with the South Pole Telescope (Vieira et al. 2010), but this has a much larger beam size ($\simeq 60$ arcsec) and much lower sensitivity [3.4 mJy at 1.4 mm, which corresponds to 6.5 mJy at 1.1 mm assuming the average SMG spectral energy distribution (SED) from Michałowski et al. 2010a at $z = 2$–3].

The AzTEC survey considered here incorporates the two smaller fields (totalling $\simeq 0.2\,\deg^2$) covered by the original SCUBA-SHADES 850 μm imaging. The 850 μm sources uncovered by the SCUBA (Coppin et al. 2006) have already been the subject of extensive multifrequency analysis, including the identification (ID) of their galaxy counterparts via radio (VLA 1.4 GHz) and mid-infrared (hereafter mid-IR) (*Spitzer* 24 μm) imaging (Ivison et al. 2007), estimation of their redshifts from the observed submm–radio SEDs (Aretxaga et al. 2007), further redshift estimation and stellar mass determination based on the optical–IR data (Takagi et al. 2007; Clements et al. 2008; Dye et al. 2008), follow-up imaging at 350 μm (Coppin et al. 2008), and studies of their environments and clustering (van Kampen et al. 2005; Serjeant et al. 2008). Individual SHADES sources have also been the subject of detailed high-resolution follow-up with the SMA (Younger et al. 2008; Hatsukade et al. 2010) and with *Spitzer* mid-IR spectroscopy (Coppin et al. 2010). A final analysis of the redshift distribution and properties of the SCUBA-SHADES galaxies will be presented in Schael et al. (in preparation).

As is well known, the large beams delivered by current single-dish (sub)mm facilities hamper the search for robust counterparts at other wavelengths. Usually the radio observations are used, both because the radio emission is believed to be related to the far-IR emission (e.g. Condon 1992) and because the surface number density of

bright radio sources is relatively low (and hence associations are often unique and statistically significant). Experience has shown that radio IDs can typically be secured for $\simeq 30$–70 per cent of SMGs; the precise percentage depends on the relative depths of the (sub)mm and radio data (Ivison et al. 2002, 2007; Dannerbauer et al. 2004, 2010; Pope et al. 2006; Chapin et al. 2009; Aretxaga et al. 2011; Biggs et al. 2011; Chapin et al. 2011; Wardlow et al. 2011), with completion rates of up to 80 per cent being achieved for the relatively bright ($S_{1.1\,mm} > 4$ mJy) and/or possibly lensed samples of Ivison et al. (2005) and Wagg et al. (2009). Recently Lindner et al. (2011) obtained a 93 per cent ID rate for a sample of 41 SMGs using very deep radio data. Attempts have been made to boost the ID fraction further using, for example, *Spitzer* MIPS 24 μm data, but these have generally resulted in only a modest increase in the number of secure galaxy counterparts (Ivison et al. 2007). It has also been shown that for 30–60 per cent of SMGs (depending on depth) one can obtain 3–8 μm counterparts using the *Spitzer*/IRAC data (Ashby et al. 2006; Pope et al. 2006; Biggs et al. 2011).

The objective of this paper is to provide secure IDs and photometric redshifts for as many as possible of the 148 AzTEC-SHADES 1.1 mm sources, exploiting not only the latest extremely-deep VLA/GMRT radio and *Spitzer* MIPS 24 μm data, but also the deep *Spitzer* IRAC 8 μm maps, and the ever-improving optical–near-IR imaging which has now been secured within both the UDS/SXDF and the Lockman Hole East fields. There are two reasons to expect that we should be able to secure a higher ID fraction for the AzTEC-SHADES sample than has been obtained for any previous large (>100 sources) and complete sample of (sub)mm sources. The first is that our 1.1 mm source sample is relatively bright[1] and so we are not probing the faint part of the high-redshift (sub)mm luminosity function. The second is that, over the required $\simeq 0.7\,deg^2$ area, the radio, mid-IR and near-IR/optical data are among some of the deepest currently available. These considerations have encouraged us to try to refine the use of mid-IR data and optical–IR colour information to maximize the completeness of the galaxy IDs and hence the inferred redshift distribution of the AzTEC 1.1 mm sources.

Here we present the final results of this ID analysis, and derive photometric redshifts for the galaxies in the resulting near-complete SMG sample. We explore the implications of the inferred redshift distribution of this SMG sample, comparing it with redshift distributions previously reported from other, smaller, mm-wavelength surveys. We also explore the consistency of the redshift distributions of the AzTEC sources found in the two separate SHADES survey fields, as well as compare the AzTEC source redshift distribution with that already derived for the SCUBA 850 μm sources. Further analysis of the full SEDs of the AzTEC sources, including derived physical properties such as star formation rates (SFRs) and stellar masses, is deferred to a future paper.

This paper is structured as follows. In Section 2, we summarize the available multiwavelength data. Then, in Section 3, we describe the methods used to identify potential galaxy counterparts at other wavelengths, and to assess their statistical significance/robustness. The resulting galaxy IDs, photometric redshifts

and optical–IR SEDs are presented in Sections 4, 5 and 6, respectively, with notes on individual sources provided in Appendix A. In Section 7, we explore the implications of the derived redshift distributions, and assess the evidence for large-scale structures with the aid of simulated AzTEC surveys extracted from cosmological simulations. Section 8 closes with our conclusions. We use a cosmological model with $H_0 = 70\ km\ s^{-1}\ Mpc^{-1}$, $\Omega_\Lambda = 0.7$ and $\Omega_m = 0.3$, and give all magnitudes in the AB system.

2 DATA

We utilized the JCMT/AzTEC 1.1 mm maps and catalogues from Austermann et al. (2010).[2] These data cover $0.7\ deg^2$ to an rms depth of 0.9–1.7 mJy beam^{-1}. We selected all 148 sources presented by Austermann et al. (2010) with signal-to-noise ratios (S/Ns) > 3.5, and adopted the statistically deboosted 1.1 mm flux densities.

The VLA 1.4 GHz and GMRT 0.61 GHz radio data were taken from Ivison et al. (2005, 2007) and Ibar et al. (2009, 2010), respectively. The 1σ rms depths at the centre of the radio images are 6 and 9 μJy beam^{-1} for the 1.4 GHz maps in the Lockman Hole East and the UDS fields, respectively, and 15 μJy beam^{-1} for the 0.61 GHz map in the Lockman Hole field. Both the VLA and the GMRT radio imaging delivered a beam size of 5 arcsec (FWHM). The catalogues include sources for which >3σ detections were obtained.

The mid-IR *Spitzer* data in the Lockman Hole East field are from programmes PID 81 (PI: G. Rieke) and PID 50249 (PI: E. Egami), described in Egami et al. (2004) and Dye et al. (2008), whereas in the UDS field the mid-IR data are from the Spitzer Public Legacy Survey of the UKIDSS UDS (PI: J. Dunlop)[3] described in Caputi et al. (2011).

The optical data in both fields were obtained with Subaru/SuprimeCam (Miyazaki et al. 2002), as described in Dye et al. (2006) and Furusawa et al. (2008). The near-IR data in both fields are provided by the UKIRT Infrared Deep Sky Survey (UKIDSS; Lawrence et al. 2007) with the SXDF/UDS field benefitting from the ultradeep *J*, *H*, *K* coverage provided by the UDS (e.g. Cirasuolo et al. 2010), while the Lockman Hole East field is part of the somewhat shallower UKIDSS DXS (Warren et al. 2007).

The depths of the data in both fields are summarized in Table 1.

3 IDENTIFICATION METHOD

3.1 Radio and 24 μm IDs

We obtained the radio and 24 μm counterparts applying the method outlined in Downes et al. (1986), Dunlop et al. (1989) and Ivison et al. (2007). The 2.5σ search radius r around each AzTEC position was determined on the basis of the deboosted S/N: $r = 2.5 \times 0.6 \times$ FWHM/(S/N), where FWHM $= 18$ arcsec is the size of the beam delivered by the JCMT at 1.1 mm. In order to account for systematic astrometry shifts (due to either pointing inaccuracies or source blending; e.g. Dunlop et al. 2010), we used a minimum search radius $r = 8$ arcsec whenever the above formula produced $r < 8$ arcsec (this proved necessary for only 20 AzTEC sources).

The statistical significance of each potential counterpart was assessed on the basis of the corrected Poisson probability p that

---

[1] The rms of the AzTEC 1.1 mm data in the SHADES fields is 0.9–1.7 mJy (Austermann et al. 2010), that is, a factor of $\simeq 2$ shallower than for the AzTEC survey of the GOODS-S field (rms 0.48–0.73 mJy, Scott et al. 2010) and for the LESS survey of the ECDF-S (rms 1.2 mJy at 870 μm, Weiß et al. 2009, corresponding to 0.6–0.7 mJy at 1.1 mm assuming the average SMG SED from Michałowski et al. (2010a) at $z = 2$–3).

[2] The fluxes have been recently revised by Downes et al. (2012), but this change does not have any significant impact on our analysis.
[3] http://ssc.spitzer.caltech.edu/spitzermission/observingprograms/legacy/spuds/

Table 1. The 3σ depths of the multifrequency data used in the Lockman Hole East and SXDF/UDS fields.

Filter	Lockman Hole	UDS	Unit
B	27.4	28.8	AB mag
R	26.4	28.1	AB mag
i	26.3	27.8	AB mag
z	25.6	26.9	AB mag
J	22.9	25.5	AB mag
H	...	24.8	AB mag
K	23.5	25.2	AB mag
$3.6\,\mu m$	0.8	1.4	μJy
$4.5\,\mu m$	1.6	1.5	μJy
$5.6\,\mu m$	11	19	μJy
$8.0\,\mu m$	13	12	μJy
$24\,\mu m$	25	30	μJy
1.1 mm	0.9–1.3	1.0–1.7	mJy
1.4 GHz	18	27	μJy
0.6 GHz	45	...	μJy

the chosen radio or 24 μm candidate could have been selected by chance.

3.2 IRAC 8 μm IDs

In order to maximize the fraction of AzTEC galaxies with identified counterparts, we also explored other ways to select IDs.

There is now a growing body of evidence indicating that SMGs are bright at the rest-frame near-IR wavelengths (Ashby et al. 2006; Pope et al. 2006; Hainline et al. 2009; Biggs et al. 2011; Wardlow et al. 2011) and hence are expected to be massive (Borys et al. 2005; Michałowski et al. 2010a,b, 2012; Hainline et al. 2011; Bussmann et al. 2012; Yun et al. 2012). Similarly to Ashby et al. (2006), we thus explored the potential of using the available IRAC 8.0 μm imaging to search for IDs. We used the longest IRAC wavelength because the surface density of bright sources is lower than at shorter wavelengths.

We selected the 8 μm IDs in a similar way to the radio and 24 μm IDs, that is, we searched for 8 μm objects within the same search radius, and estimated the probability of a chance association using analogous p statistics. To do this we derived the cumulative number counts of 8.0 μm sources in our fields; we found that this had the form $N(>S_{8.0}) \propto S_{8.0}^{-1.1}$ with a normalization given by $N(>20\,\mu\text{Jy}) = 4\,\text{arcmin}^{-2}$. We did not select candidate IDs at flux densities fainter than 20 μJy.

3.3 Red $i - K$ IDs

It is now well known that SMGs generally exhibit red optical/near-IR colours (Smail et al. 1999, 2002, 2004; Ivison et al. 2002; Webb et al. 2003; Dannerbauer et al. 2004; Ashby et al. 2006; Yun et al. 2012). This is likely a consequence of two effects: SMGs are very dusty and they host a significant evolved stellar population (Michałowski et al. 2010a, 2012). Similarly, $\simeq$60 per cent of ultra-luminous IR galaxies (ULIRGs) at $z \simeq 2$–3 are very red with $i - K > 2.5$ (Caputi et al. 2006).

Therefore, we explored the potential of red $i - K$ colour to yield SMG galaxy counterparts, building on the work of Schael et al. (in preparation).[4] Schael et al. showed, for SCUBA sources in the

[4] See also Schael (2009).

SHADES fields, that the reddest ($i - K > 2$) source within 10 arcsec of the SCUBA position usually corresponds to the radio ID. We therefore selected all sources with $i - K > 2$ within the search radius defined above, and again estimated their reliability as AzTEC IDs by estimating the a priori probability p. The number density of K-band detected sources in the magnitude range of interest is well described by Euclidean counts, with $N(>S_K) \propto S_K^{-1.5}$. We estimated the number density at $K = 23$ mag separately for sources with $i - K$ colours 2–2.5, 2.5–3 and >3 to be $N(K < 23\,\text{mag}) = 8$, 4 and 2 arcmin^{-2}, respectively. These number densities were used to calculate the p values for sources with $i - K$ colours of 2–2.5, 2.5–3 and >3, respectively. We did not select sources fainter than $K = 23$ mag.

4 IDENTIFICATIONS

In Figs B1 and B2, we present thumbnail images for all the AzTEC-SHADES sources, with the IDs indicated by coloured symbols. For completeness and future reference, Tables B3 and B4 give the positions, relevant flux densities, angular offsets (from the original AzTEC 1.1 mm positions), and probabilities of chance associations (p) for all candidate radio and 24 μm IDs, regardless of their p values. When IDs obtained at different wavelengths were separated by less than 2.5 arcsec, they are listed as a single ID. Tables B1 and B2 present the relevant data only for the reliable IDs with $p < 0.05$ (marked in bold) and tentative IDs with $0.05 < p < 0.1$ (marked in italic). The coordinates listed are those of the 1.4 GHz ID if present, or alternatively those of the appropriate 24 μm (or 0.61 GHz), 8 μm or $i - K$ selected ID.

We matched these coordinates with the optical/near-IR catalogues, using a matching search radius of $r = 1.5$ arcsec. The resulting multiwavelength photometry was used both to derive photometric redshifts for the IDs (Section 5) and to select additional IDs as described above. Specifically, using the method presented in Section 3.2 we selected nine (five) additional IDs in the Lockman Hole field (UDS field) from the IRAC 8.0 μm imaging. For two (one) of the AzTEC-SHADES sources, these are the only IDs, so this method adds a very small, but still useful set of extra IDs. We checked the 22 AzTEC sources for which we found both robust radio ($p < 0.05$) and 8.0 μm IDs, and found that they coincided in 20 cases (91 per cent), providing additional confidence that the 8.0 μm method can be reliably utilized when the radio data are not deep enough.

In addition, using the method presented in Section 3.3 we identified 16 (28) significant $i - K$ colour-selected IDs in the Lockman Hole field (UDS field). For one (five) of the AzTEC-SHADES sources these are the only IDs, so again the result of this effort is another small, but helpful set of additional IDs, along with supporting evidence for several others. Again we checked the AzTEC sources for which we found both robust radio and $i - K$ IDs, and found that they agreed in 19/23 cases (83 per cent), providing the reassurance that the $i - K$ method can be reliably used when the radio data are not deep enough.

The final success rate of source ID is summarized in Table 2. The IDs have been divided into three categories. Category 1 is used for an ID which has a very low probability of chance association, $p < 0.05$ (p marked as bold in Tables B1 and B2 and a big symbol in Figs B1 and B2). Category 2 denotes an ID selected at least twice by one of the radio, 24 μm 8.0 μm or $i - K$ methods with $0.05 < p < 0.1$, while category 3 indicates an ID that has been selected by only one of these methods with $0.05 < p < 0.1$.

Table 2. The success rate of the ID process. The columns show: (1) the field name; (2) the total number of AzTEC sources; (3) the number of sources with IDs having at least one association with $p < 0.05$ at radio, 24 μm, 8.0 μm or $i - K$; (4) the number of sources with IDs having at least two associations with $0.05 < p < 0.1$; (5); the number of sources with IDs having only one potential counterpart with $0.05 < p < 0.1$; (6) the number of sources with no IDs; (7) the total number of sources covered by the optical map (i.e. those for which a photometric redshift could in principle be reliably estimated); (8) the number (and percentage relative to the number of sources covered by the optical map) of sources with an optical–near-IR photometric redshift; (9) the number of sources with category 1 and an optical–near-IR photometric redshift.

Field (1)	N (2)	Category 1 (3)	Category 2 (4)	Category 3 (5)	No ID (6)	N_{opt} (7)	z_{opt} (8)	Category 1 with z_{opt} (9)
Lockman Hole	91	64 (70 per cent)	7 (8 per cent)	7 (8 per cent)	13 (14 per cent)	62	47 (76 per cent)	39 (63 per cent)
UDS	57	31 (54 per cent)	1 (2 per cent)	8 (14 per cent)	17 (30 per cent)	44	31 (70 per cent)	24 (55 per cent)
Both	148	95 (64 per cent)	8 (5 per cent)	15 (10 per cent)	30 (20 per cent)	106	78 (74 per cent)	63 (59 per cent)

The higher category 1 rate for the Lockman Hole can be primarily attributed to the slightly deeper radio data available in this field. Indeed, if the radio depth were degraded to the same as that available in the UDS field ($\simeq 45$ μJy, 5σ), then the category 1 ID percentage in the Lockman Hole field would drop to 58 per cent, very similar to that found within the UDS field. The impact of the depth of the radio data on the ID rate is further demonstrated by the fact that the final total AzTEC-SHADES SMG ID rate of $\simeq 80$ per cent is surpassed only by the survey of Lindner et al. (2011), who benefitted from the ultra-deep radio data available only in the Lockman Owen field, which reaches down to an rms $\sigma_{1.4\,GHz} \simeq 2.7$ μJy in the central regions.

The ID success rate separately for each method is shown in Table 3. The radio and 24 μm methods in the Lockman Hole field deliver higher success rates than in the UDS field due to deeper data in the former field (see Table 1). On the other hand, deeper optical data in the UDS field do not help to increase the success rate for the $i - K$ method. This is because no $i - K$ ID in the UDS field is fainter than the 3σ limit of $K = 23.5$ mag in the Lockman Hole field. However, deeper data in the UDS field help to increase the fraction of IDs with redshifts (see Table 2).

To determine the redshift distribution of the AzTEC-SHADES sources, we decided to select only one ID for each source. For the vast majority of cases this is straightforward. However, for some sources there is more than one apparently significant galaxy counterpart. To deal with these cases, we adopted a policy of selecting the ID with the greatest number of high-significance ($p < 0.05$) entries in Tables B1 and B2 or, if IDs have only been uncovered at a single wavelength, the ID with the lowest value of p. If this procedure did not select a single ID, then we looked for the ID with the greatest number of moderate-significance ($0.05 < p < 0.1$) entries. In principle, such multiple IDs may indicate that the AzTEC source is a blend of a few galaxies (e.g. Wang et al. 2011); higher resolution submm imagining is necessary to test this.

The frequency of multiple IDs is $\simeq 21 \pm 5$ per cent (19/91) for the Lockman Hole and $\simeq 11 \pm 4$ per cent (6/57) for the UDS field, where the errors reflect the Poissonian uncertainties. This is consistent with the rates found for SCUBA sources in the same fields ($\simeq 9 \pm 5$ per cent, Clements et al. 2008; $\simeq 19 \pm 5$ per cent, Ivison et al. 2007) and for AzTEC sources in the GOODS-N ($\simeq 18 \pm 8$ per cent, Chapin et al. 2009) and GOODS-S ($\simeq 10 \pm 5$ per cent, Yun et al. 2012) fields.

We identified two sources (AzUDS5 and 43) with statistically robust IDs corresponding to optically-bright galaxies with very low photometric redshifts ($z \simeq 0.45$ and $z \simeq 0.15$, respectively). Such low redshifts are completely inconsistent with their 1.1 mm-to-24 μm flux density ratios for any known long-wavelength SED (see Fig. 1). In the case of AzUDS5, the angular offset between the radio position

and the optical galaxy is 0.65 arcsec, suggesting that this is an example of galaxy lensing, and that the SMG lies at much higher redshift (e.g. Dunlop et al. 2004). We note this, but leave the redshift as it is since we do not currently possess any CO spectroscopy of this source which might help to determine the true redshift of this SMG (see e.g. Negrello et al. 2010). However, in the case of AzUDS43 we have identified a second, statistically-robust ID at $z \simeq 2.43$, 3.5 arcsec away from the bright low-redshift optical ID, and so we have adopted this ID and its photometric redshift in the determination of the redshift distribution.

To test the reliability of the IDs, in Fig. 2 we show the distribution of the offsets of IDs from the AzTEC positions. Similarly to Biggs et al. (2011), we fitted the Rayleigh distribution, $R(r) \propto r \exp(-r^2/2\rho^2)$, expected to explain the data if offsets originate from the statistical positional uncertainty of the AzTEC sources. For each ID the value of the offset is normalized to the 1σ AzTEC positional uncertainty equal to $\sigma = 0.6 \times$ FWHM/(S/N) (Section 3.1). Hence, the value of ρ corresponds to the 1σ positional uncertainty of IDs expressed in the units of such calculated σ and hence should be equal to 1. The derived values are lower, so likely our estimates of the AzTEC positional uncertainties are overestimated. This is not because for 20 sources we reset the search radius to 8 arcsec (2.5σ; Section 3.1), as after we remove this limit the values of ρ increase only by <0.05. There is an indication that the distributions of all IDs exhibit a slight excess at higher offsets compared to the model and to the robust-only IDs, indicating that some of the category 2 and 3 IDs are not correct, but this difference is not statistically significant. From the reduced χ^2 values we conclude that the offset distributions are consistent with the Rayleigh distribution, so the number of wrongly assigned IDs is small (as they should manifest themselves as a significant signal at larger offsets).

5 REDSHIFTS

We have used the photometric redshift catalogues from Cirasuolo et al. (2007, 2010) and McLure et al. (2009) in the UDS field and have now produced an equivalent catalogue in the Lockman Hole East field, albeit with larger uncertainties due to the shallower near-IR data. All optical, near-IR and IRAC data were used in the fits. These catalogues have been produced using the HYPERZ package (Bolzonella, Miralles & Pelló 2000) with the stellar population models of Bruzual & Charlot (2003) and a Chabrier (2003) initial mass function with a mass range 0.1–100 M$_\odot$. A double-burst star formation history was assumed, but this choice has little impact on derived redshifts (as opposed to derived stellar masses; Michałowski et al. 2012). The metallicity was fixed at the solar value and reddening was calculated following the Calzetti et al. (2000) law within

Table 3. The success rate of the ID process for the five individual methods. The columns show: (1) field name; (2) the total number of AzTEC sources; (3) the number of sources with any 1.4 GHz ID; (4) the number of sources with a category 1 1.4 GHz ID; (5) and (6) any/category 1 0.6 GHz IDs; (7) and (8) any/category 1 24 µm IDs; (9) the number of sources covered by the IRAC map; (10) and (11) any/category 1 8.0 µm IDs; (12) the number of sources covered by the i- and K-band maps; (13) and (14) any/category 1 $i - K$ IDs.

| Field | N | 1.4 GHz IDs | | 0.6 GHz IDs | | 24 µm IDs | | N | 8.0 µm IDs | | N | $i - K$ IDs | |
		Any	Category 1	Any	Category 1	Any	Category 1		Any	Category 1		Any	Category 1
(1)	(2)	(3)	(4)	(5)	(6)	(7)	(8)	(9)	(10)	(11)	(12)	(13)	(14)
Lockman Hole	91	66 (73 per cent)	50 (55 per cent)	57 (63 per cent)	46 (51 per cent)	63 (69 per cent)	43 (47 per cent)	64	35 (55 per cent)	24 (38 per cent)	54	26 (48 per cent)	18 (33 per cent)
UDS	57	25 (44 per cent)	21 (37 per cent)	N/A	N/A	22 (39 per cent)	16 (28 per cent)	51	14 (27 per cent)	5 (10 per cent)	44	23 (52 per cent)	13 (30 per cent)
Both	148	91 (61 per cent)	71 (49 per cent)	N/A	N/A	85 (57 per cent)	59 (40 per cent)	115	49 (43 per cent)	29 (25 per cent)	98	49 (50 per cent)	31 (32 per cent)
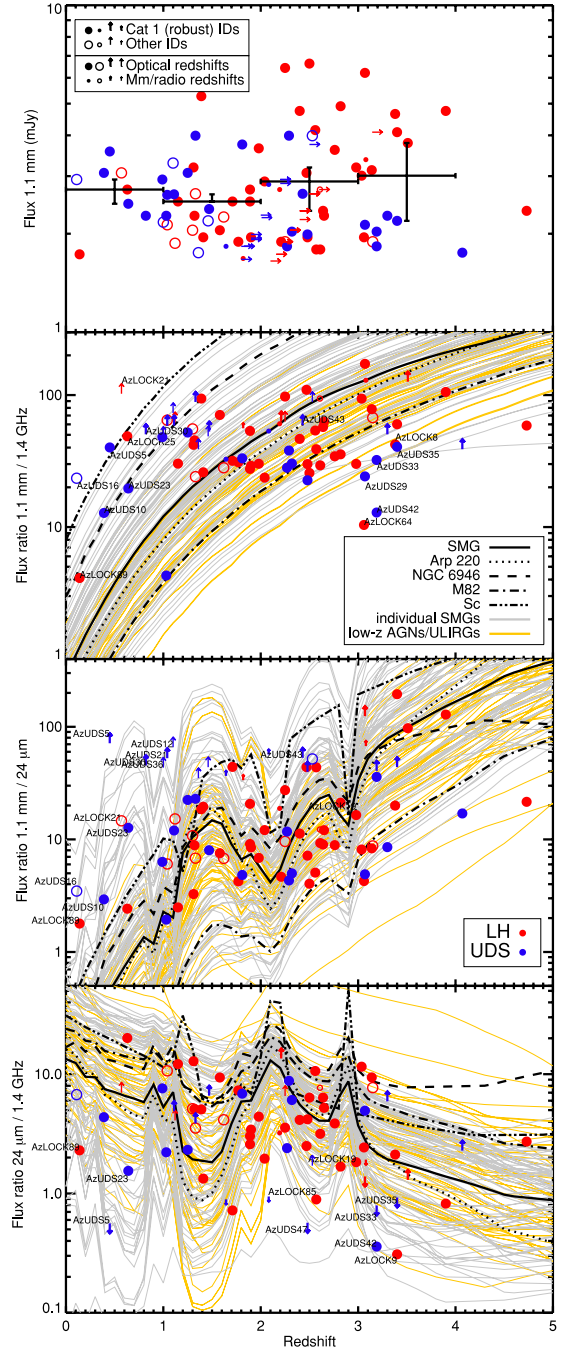
Figure 1. 1.1 mm flux densities (medians in four redshift bins with 68 per cent bootstrap errors are shown as the thick crosses) and the 1.1 mm-to-1.4 GHz, 1.1 mm-to-24 µm and 24 µm-to-1.4 GHz flux density ratios plotted against redshift for all the AzTEC-SHADES sources (the best ID is shown for each source) presented in Tables B1 and B2 (colour symbols – red: Lockman Hole field; blue: UDS field). The circles denote detections at both bands, whereas the upward and downward arrows denote non-detections at one of the wavelengths. The filled circles and thick arrows indicate category 1 (robust; $p < 0.05$) IDs, whereas the open circles and thin arrows indicate other IDs. The big symbols indicate sources with optical–near-IR photometric redshifts, whereas the small symbols indicate that the 1.1 mm-to-1.4 GHz flux density ratio redshift estimator was used due to a lack of optical/IR photometry. For comparison, the predicted redshift evolution of the flux density ratios calculated using the SEDs of an average SMG and individual SMGs (Michałowski et al. 2010a), of local galaxies (Silva et al. 1998) and local ULIRGs/AGNs (Vega et al. 2008) are shown (lines).
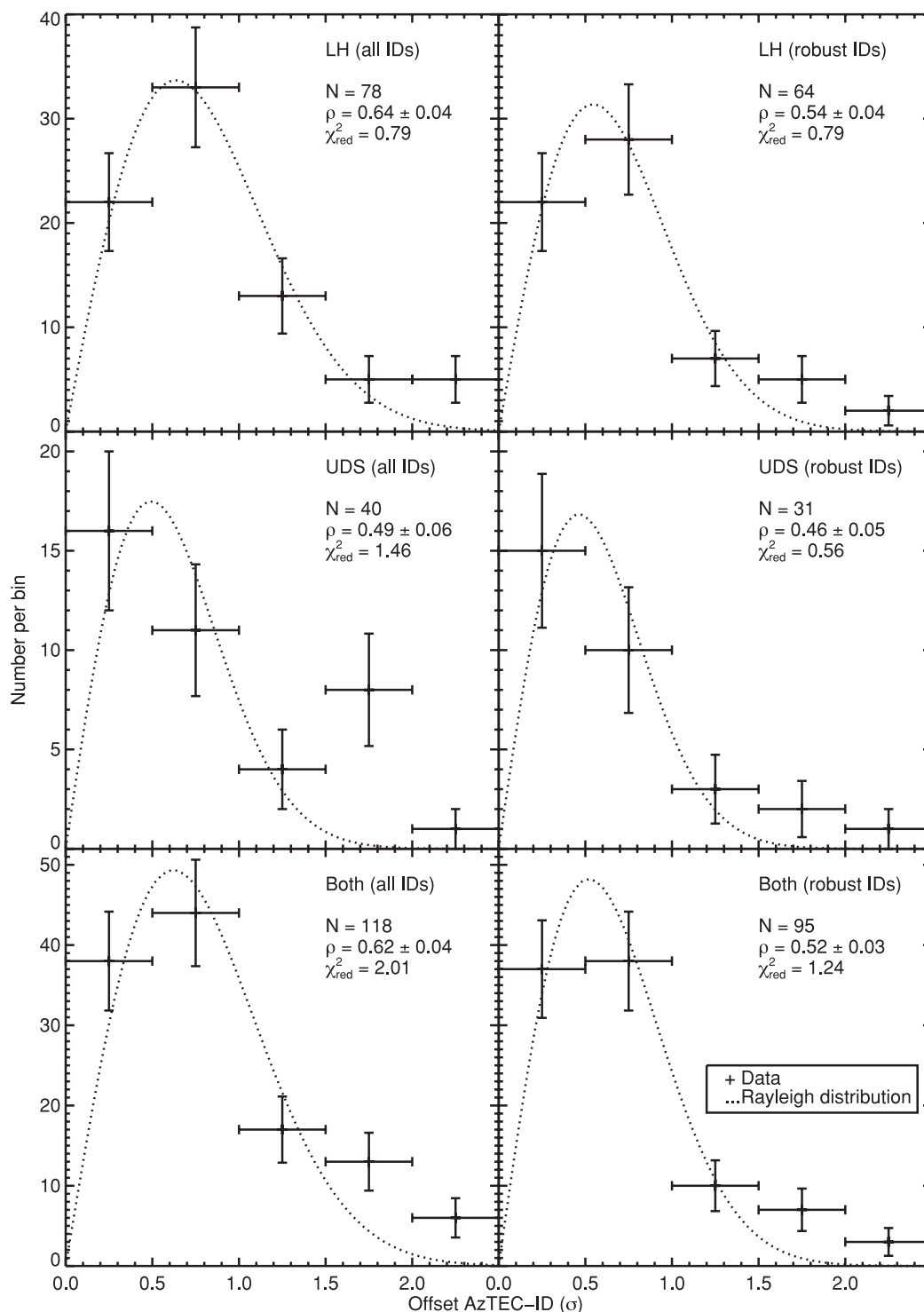
Figure 2. Distribution of the offsets of IDs from the AzTEC positions (crosses with Poissonian error bars; only the best ID is taken into account for each source) and the Rayleigh distribution (dotted lines), $R(r) \propto r \exp(-r^2/2\rho^2)$, expected to explain the data if offsets originate from the statistical positional uncertainty of the AzTEC sources. Each panel represents all or robust (category 1, $p < 0.05$) IDs in the Lockman Hole field or in the UDS field or both. As in Biggs et al. (2011), for each ID the value of the offset is normalized to the 1σ AzTEC positional uncertainty, $\sigma = 0.6 \times$ FWHM/(S/N) (Section 3.1). Hence, the value of ρ corresponds to the 1σ positional uncertainty of IDs expressed in the units of such calculated σ and hence should be equal to 1. The numbers given in each panel are lower, so likely our estimates of the AzTEC positional uncertainties are overestimated. This is not because for 20 sources we reset the search radius to 8 arcsec (2.5σ; Section 3.1), as after we remove this limit the values of ρ increase only by <0.05. There is an indication that the distributions of all IDs exhibit a slight excess at higher offsets compared to the model and to the robust-only IDs, indicating that some of the category 2 and 3 IDs are not correct, but this difference is not statistically significant. For each panel the number of IDs and the reduced χ^2 of the fit of the Rayleigh distribution to the data are shown indicating that the offset distributions are consistent with the Rayleigh distribution, so the number of wrongly assigned IDs is small (as they should manifest themselves as a significant signal at larger offsets).

the range $0 \leq A_V \leq 6$. The H I absorption along the line of sight was included according to the prescription of Madau (1995).

The resulting photometric redshifts are given in Tables B1 and B2. For sources with multiple IDs, the ID used in the determination of the redshift distribution is marked in bold (see Section 4). For sources with no optical–IR photometric redshift we provide a redshift estimate based on the 1.1 mm-to-1.4 GHz ratio (shown in italics), adopting the average SED of SMGs from Michałowski et al. (2010a).

AzUDS48 is not covered by the radio map, so an estimate of its redshift has been deduced from its 1.1 mm-to-24 μm flux density ratio (see the third panel of Fig. 1).

The accuracy of the photometric catalogue of Cirasuolo et al. (2010) is excellent, with a mean $\Delta z/(1 + z_{\rm spec}) = 0.008 \pm 0.034$. For nine AzTEC sources with spectroscopic redshift (see Appendix A) we derived a mean $\Delta z/(1 + z_{\rm spec}) = -0.06 \pm 0.20$, also consistent with zero.

The median redshift (and 68 per cent bootstrap error) of AzTEC-SHADES sources in the Lockman Hole field is $z_{\rm med} \simeq 2.25^{+0.25}_{-0.21}$, in the UDS field it is $z_{\rm med} \simeq 1.64^{+0.63}_{-0.28}$, and for the full combined sample it is $z_{\rm med} \simeq 2.19^{+0.10}_{-0.30}$.

To date, only 11 SMGs have been shown to lie at $z > 4$ (Capak et al. 2008, 2011; Knudsen, Kneib & Egami 2008; Schinnerer et al. 2008; Coppin et al. 2009; Daddi et al. 2009a,b; Knudsen et al. 2010; Riechers et al. 2010; Cox et al. 2011; Smolčić et al. 2011; Combes et al. 2012; Walter et al. 2012). We have identified five AzTEC-SHADES sources ($\simeq$5 per cent) with photometric redshifts $z \gtrsim 4$ (AzLOCK6, AzLOCK38, AzUDS11, AzUDS32, AzUDS54). However, for all of these galaxies the uncertainties in the photometric redshifts are significant, and lower redshift ($z \simeq 2$) solutions cannot be excluded. In addition, several AzTEC sources that are unambiguously detected in the radio (and in some cases also at 8.0 μm) remain undetected in the optical imaging (AzLOCK36, AzLOCK38, AzLOCK71, AzLOCK81, AzLOCK91, AzUDS25, AzUDS40 and AzUDS57). These sources are thus also candidates for very high redshift (or highly dust obscured) galaxies.

The success rate of redshift determination is summarized in Table 2 (column 8). Excluding AzTEC sources that are not covered by the necessary optical–IR data, we obtained optical photometric redshift estimates for $\simeq$75 per cent of sources or $\simeq$60 per cent if only category 1 IDs are taken into account (i.e. out of the 106 AzTEC sources which lie within the area covered by the deep optical/near-IR imaging, we obtained optical photometric redshift estimates for 78; out of them 63 have category 1 IDs). This is the most complete redshift information achieved to date for an unbiased sample of SMGs. For the remaining 28 ($\simeq$25 per cent) SMGs no ID was selected, or the radio ID does not possess an optical counterpart, so the optical redshift could not be obtained.

The redshift distribution of the AzTEC-SHADES sources is shown in Fig. 3, where it is compared with that displayed by similar (but smaller) samples of SMGs selected in the GOODS-N (Chapin et al. 2009) and GOODS-S (Yun et al. 2012), as well as with the spectroscopically determined redshift distribution of a somewhat heterogeneous selection of 850-μm-selected galaxies reported by Chapman et al. (2005). The redshift distribution of the AzTEC-SHADES sources is peaked at $z \simeq 2$–2.5, but has a high-redshift tail (extending to at least $z \simeq 4$) as well as a significant intermediate-redshift population.

As perhaps expected, the redshift distribution of AzTEC-SHADES sources is similar to that previously derived for 850-μm-selected galaxies, and to that displayed by the AzTEC-ASTE sample in the GOODS-S; the Kolmogorov–Smirnov (KS) test
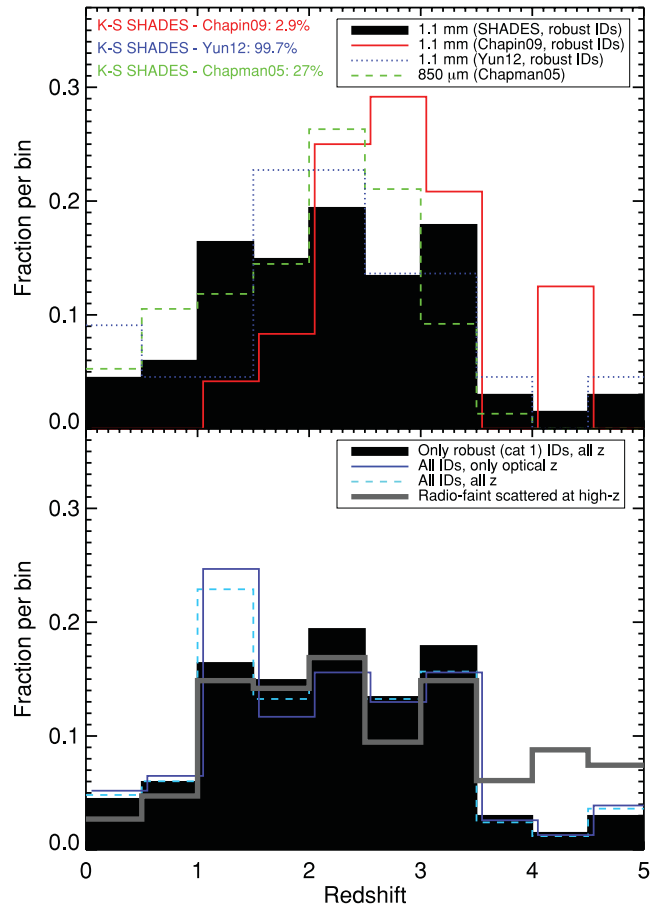

Figure 3. Upper panel: the redshift distribution of 1.1-mm-selected galaxies in the SHADES fields with robust ($p < 0.05$) IDs using optical–near-IR and 1.1 mm-to-1.4 GHz flux density ratio redshifts (solid black histogram). In this plot, any sources which only possess lower limits to their estimated redshifts have been excluded. Also shown are the redshift distributions of the 1.1-mm-selected galaxies in the GOODS-N (solid red line; Chapin et al. 2009) and the GOODS-S (dotted blue line; Yun et al. 2012), as well as the spectroscopically determined redshift distribution of 850-μm-selected galaxies reported by Chapman et al. (2005, green dashed line). The distributions peak at $z \simeq 2$–3 but contain objects over the redshift range $z \simeq 0$–4. The KS test probabilities that samples are consistent with being drawn from the same parent population are indicated. The apparent difference at low redshifts between the SHADES and GOODS-N samples can be explained by the relatively small area of the latter survey (see Fig. 4 and Section 5). Lower panel: an exploration of the robustness of the SHADES-AzTEC redshift distribution. The redshift distribution of the same set of robust IDs is again shown by the solid black histogram. The solid blue line represents only those IDs with optical–near-IR photometric redshifts, while the dashed cyan line includes all IDs, irrespective of robustness (i.e. including categories 1, 2 and 3) and the type of redshift. The grey thick line shows the redshift distribution for all AzTEC-SHADES SMGs, this time including those not detected at radio or optical wavelengths, which were scattered between $z = 5$ and the lower limit derived from the 1.1 mm-to-1.4 GHz flux density limit using the SMG SED template from Michałowski et al. (2010a).

indicates that the redshift distribution of the AzTEC-SHADES sources and that reported by Chapman et al. (2005) and Yun et al. (2012) are consistent with the hypothesis that all three samples are drawn from the same parent population (Fig. 3).

However, our redshift distribution is slightly different from that reported by Chapin et al. (2009) in the GOODS-N. The KS test

yields a probability of only $p \simeq 2.9$ per cent that the AzTEC-SHADES and GOODS-N AzTEC samples are drawn from the same population (i.e. the difference is at the 2.2σ level). The probability increases to $\simeq 15$ per cent (no significant difference) when $z < 1$ SMGs in the AzTEC-SHADES sample are removed.

To further explore the likelihood of this difference, we divided each of our fields into four equal parts, each similar in size to the GOODS-N field, and analysed their redshift distributions separately (see Figs 4 and 7). We found that in 50 per cent (4/8) of such small fields we did not detect any $z < 1$ source. To confirm this we performed a Monte Carlo simulation by selecting in both of our fields 100 000 randomly located subfields with areas equal to that of Chapin et al. (2009). We found that $\simeq 60$ per cent of these subfields did not contain any $z < 1$ object. This suggests that the sample of Chapin et al. (2009) may miss the lower redshift population due to its small area and advocates for using larger fields to obtain a representative sample of mm-selected galaxies. Further support for field-to-field variation is provided by the differences in mm number counts in different fields, in particular by the fact that the GOODS-N field has systematically higher number counts compared to other fields (Scott et al. 2010, 2012).

The lower panel of Fig. 3 shows that the form of the derived redshift distribution is essentially unaffected by whether one restricts the redshift information to only optical–IR photometric redshifts, or alternatively includes all available redshift information (i.e. including estimates based on mm–radio colour). However, when we include the category 2 and 3 IDs, then a spike at $z \simeq 1$–1.5 appears. At least some of these less-robust IDs are likely misidentifications, because, as shown in Fig. 5, the redshift distribution of all optical/near-IR galaxies in both the survey fields peaks at $z \simeq 1$.

Fig. 6 shows the redshift distribution of the robust ($p < 0.05$) IDs of the AzTEC sources separately in the Lockman Hole and the UDS fields compared with that of the 850-μm-selected SMGs in (smaller subregions of) the same fields (Clements et al. 2008; Dye et al. 2008; Schael et al., in preparation). Applying the KS test we found that, within each field, the redshift distributions of the 1.1-mm- and 850 μm-selected populations are completely consistent (the significance values, p, are indicated in Fig. 6), although (unsurprisingly) there is a tendency for the 1.1-mm-selected SMGs to lie at slightly higher redshifts. This consistency is not driven by the fact that both populations are composed of the same galaxies; the AzTEC images cover significantly larger areas than the SCUBA maps, to somewhat shallower effective depths (and different completeness), and consequently there are only 13 and six sources in common between the 1.1-mm- and 850-μm-selected samples in the Lockman Hole and UDS fields, respectively (see Figs 4 and 7 and Appendix A). The implications of this result are explored further below in Section 7.

In principle, active galactic nucleus (AGN) contamination may influence our photometric redshift estimates, which are based on purely star forming templates. Hainline et al. (2009, 2011) claimed a significant AGN contribution to the IRAC fluxes of SMGs; however, Michałowski et al. (2012) found that the AGN contamination is unlikely to influence the SED modelling. Additionally, the photometric errors of IRAC fluxes are typically ~10 per cent, significantly larger than that of our deep optical and near-IR data, so even if the AGN contamination was significant at IRAC wavelengths, these data should not influence the derived photometric redshifts significantly. Similarly, Wardlow et al. (2011) found that the exclusion of the 8.0-μm data does not significantly change the derived photometric redshifts of SMGs.

6 FLUX RATIOS

In order to verify that these redshift estimates are consistent with the available photometry, in Fig. 1 we show 1.1 mm flux density, as well as the three flux density ratios 1.1 mm to 1.4 GHz, 1.1 mm to 24 μm and 24 μm to 1.4 GHz plotted against redshift for all the identified AzTEC-SHADES sources (utilizing the best ID for each source, determined as described above). The lower three panels also show the expected redshift dependence of the appropriate flux density ratio as predicted by the SED of an average SMG and individual SMGs (Michałowski et al. 2010a), the SEDs of local galaxies (a ULIRG, a starburst and spirals; Silva et al. 1998) and the SEDs of local ULIRGs/AGNs (Vega et al. 2008). The filled/thick symbols indicate category 1 (robust, $p < 0.05$) IDs, and the smaller symbols indicate that the 1.1 mm-to-1.4 GHz flux density ratio redshift estimator was used due to a lack of optical–IR photometry.

The top panel shows that the brightest AzTEC sources preferentially lie at higher redshifts (consistent with Ivison et al. 2002; Wall, Pope & Scott 2008; Marsden et al. 2011); all but one of the sources brighter than 4 mJy are at $z > 2$ (i.e. the upper left-hand corner of this panel is almost empty). However, this does not mean that the median flux densities of AzTEC sources is higher at higher redshifts (see the thick crosses in this panel).

For sources with no radio detections, the derived 1.1 mm-to-1.4 GHz redshifts are lower limits. As can be seen from the arrows in the top panel of Fig. 1, the derived limits do not allow us to place very strong redshift constraints on these sources (typically $z > 2$). Hence, in general, the lack of a radio detection does not imply that such sources lie at substantially higher redshifts than the radio-detected subset; given the 1.1 mm flux densities of the sources, and the depth of the available radio data, a radio-blank SMG could be at $z < 3$ or even at $z < 1.5$ if its dust is very cold (similar to spiral galaxies).

The second panel of Fig. 1 reveals the redshift dependence of the implied dust temperature of the galaxies within the AzTEC-SHADES sample (assuming the photometric redshifts are broadly correct). Namely, the 1.1 mm-to-1.4 GHz flux density ratios of the AzTEC sources do not change with redshift, implying that those at $z < 1.5$ are cooler (consistent with the SEDs of Sc spirals and NGC 6946), whereas those at higher redshifts are hotter (consistent with the SEDs of an average SMG, Arp 220 and M82).

Finally, the bottom two panels of Fig. 1 show that the vast majority of the AzTEC-SHADES sources lie within the regions spanned by the range of SED models considered (only for the sources denoted as the small symbols were the redshifts in fact derived from the fluxes plotted in this figure). This indicates that our optical photometric redshift estimates are reasonable, in the sense that they are generally consistent with the anticipated range of 1.1 mm-to-24 μm and 24 μm-to-1.4 GHz flux density ratios. We note that radio-loud AGNs from Shang et al. (2011) have 1.1 mm-to-1.4 GHz and 24 μm-to-1.4 GHz flux density ratios of 0.01–0.03 in the redshift range 0–5. Hence, the sources which lie below the SED locus in the second panel (AzLOCK64 and AzUDS42, both category 1 IDs) may be readily explained by some contribution from AGN synchrotron radiation at radio wavelengths.

7 LARGE-SCALE STRUCTURES

With only photometric redshifts it is difficult to study the large-scale structures traced by SMGs. However, as is evident from Fig. 6, the redshift distributions of the AzTEC sources in both the Lockman Hole and UDS fields are strikingly similar to that displayed by the
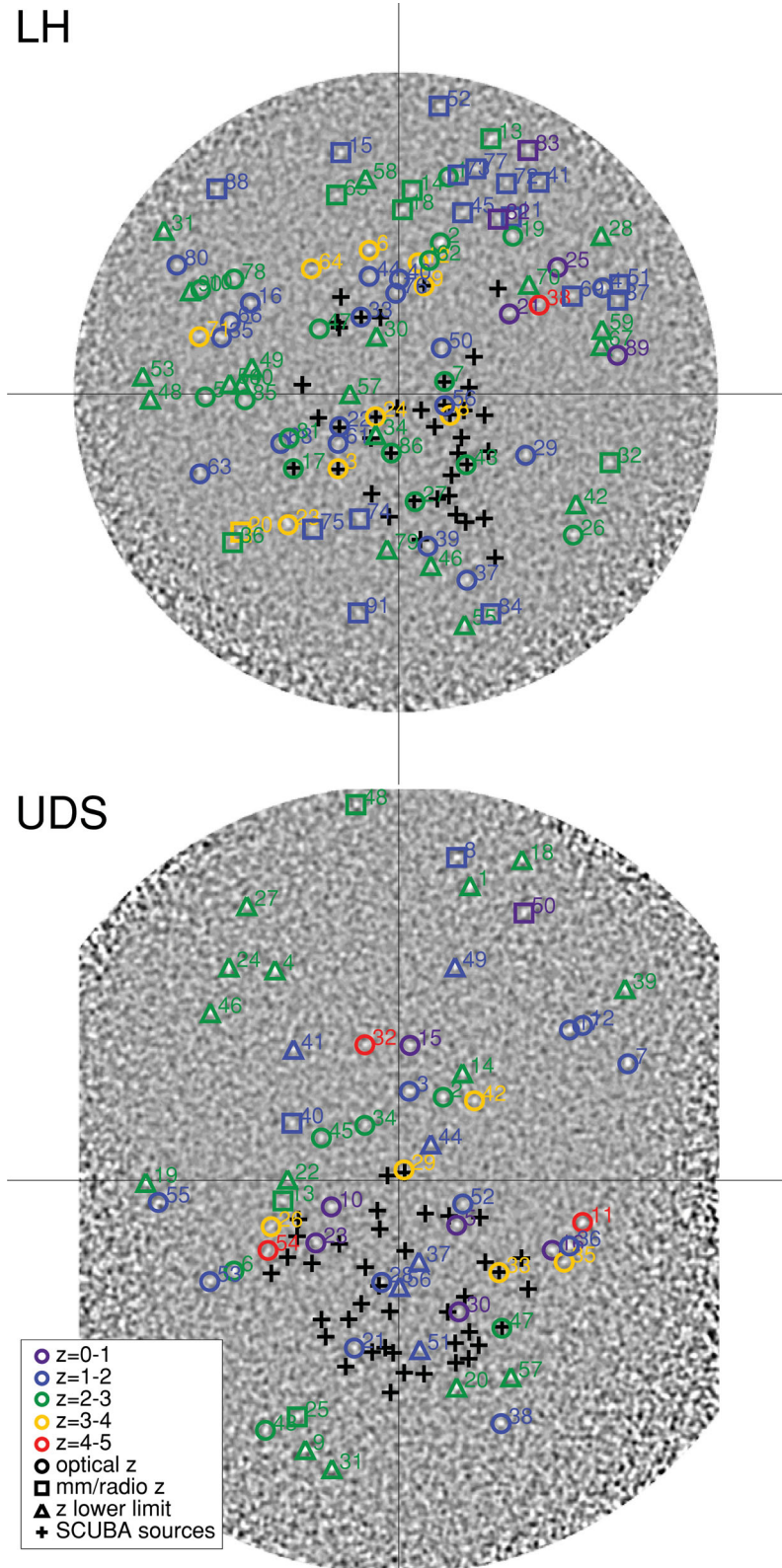
Figure 4. The AzTEC 1.1 mm maps of the Lockman Hole (top) and the SXDF/UDS (bottom) fields from Austermann et al. (2010). Both images are 0°88 on a side (the noisier edges have been removed). The sources analysed in this paper are marked and colour-coded according to their redshifts. The circles correspond to spectroscopic or photometric optical or mid-IR polycyclic aromatic hydrocarbon (PAH) redshifts, whereas the squares correspond to redshifts derived from the 1.1 mm-to-1.4 GHz flux density ratio based on the average SED model of SMGs (Michałowski et al. 2010a). In the case of a radio non-detection this method provides only a lower limit to the redshift and such cases are marked with the triangles. The black lines divide both fields into four equal parts each with an area similar to that of the GOODS-N AzTEC survey studied by Chapin et al. (2009). 50 per cent (4/8) of these subfields do not contain any low-redshift SMGs (i.e. robust IDs with $z < 1$). The crosses denote 850-μm-selected galaxies for which photometric redshifts have been derived by Schael et al. (in preparation).
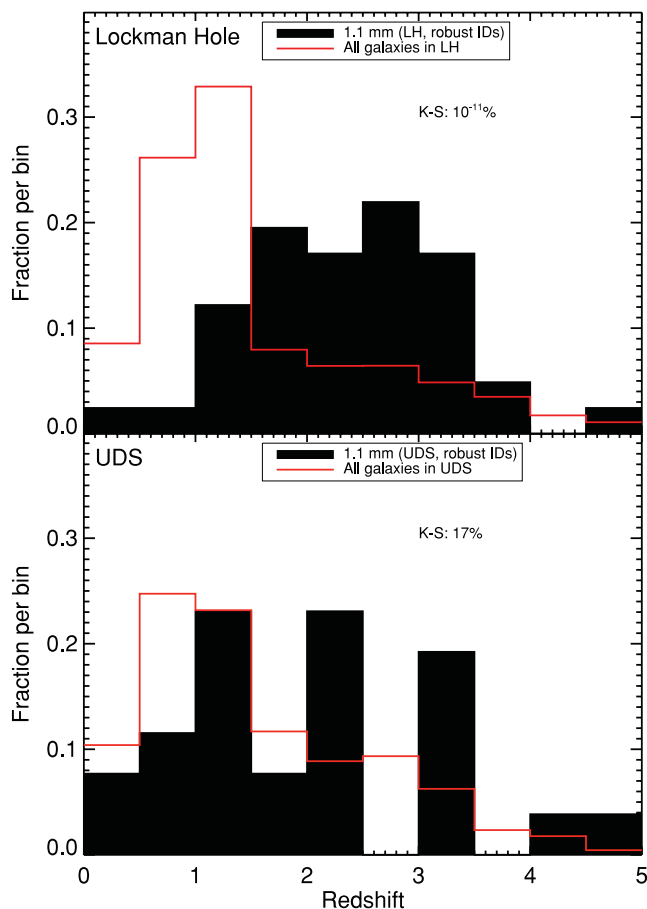
Figure 5. The redshift distribution of SHADES-AzTEC 1.1-mm-selected galaxies with robust ($p < 0.05$) IDs and either optical–near-IR or 1.1 mm-to-1.4 GHz redshifts (solid black histograms), this time shown separately for the Lockman Hole field (upper panel) and the UDS field (lower panel). Sources with only lower limits to their estimated redshifts were excluded. Also shown for comparison are the redshift distributions of all the optical/near-IR/*Spitzer* selected galaxies in the two survey fields (solid red lines). The KS test probabilities that the samples on each panel are drawn from the same parent population are indicated. The AzTEC population in the Lockman Hole field is not consistent with the general field galaxy population. The all galaxy samples (red lines) are different in both fields due to different optical depths, that is, the *i*-band data are $\simeq 1.5$ mag deeper in the UDS field (Table 1), so the high-redshift tail is much more pronounced in this field.

Figure 6. The redshift distribution of 1.1-mm-selected galaxies in the Lockman Hole (upper panel) and the UDS (lower panel) fields with robust ($p < 0.05$) IDs and optical–near-IR or 1.1 mm-to-1.4 GHz flux density ratio redshifts (solid black histograms). Sources with only lower limits to their estimated redshifts were excluded. Also shown in this figure are the redshift distributions derived for the SHADES-SCUBA 850-μm-selected galaxies in (subregions of) the same fields (robust IDs: solid red lines; all IDs: dotted red line; Dye et al. 2008; Clements et al. 2008; Schael et al., in preparation). The KS test probabilities that the samples in each panel are drawn from the same populations are indicated. The distributions of the 1.1-mm- and 850-μm-selected populations are consistent, although there is an indication that the 1.1 mm selection results in slightly higher redshifts. Combining the AzTEC and SCUBA samples in each field reveals a statistically significant difference between the inferred redshift distributions of SMGs in the Lockman Hole and UDS fields (see Section 7).

SCUBA sources in the same fields, even though SCUBA covered much smaller subregions within these fields (see Figs 4 and 7) and there are only 13 and six sources in common in the Lockman Hole and UDS samples, respectively. Indeed, the KS test shows that the AzTEC and SCUBA sources in each field are fully consistent with being drawn from the same population ($p = 61$ per cent in the Lockman Hole field and $p = 50$ per cent in the UDS field). Interestingly, this consistency between the redshift distributions of the AzTEC and SCUBA sources *within* each field is better than the consistency of the redshift distributions *between* the two SHADES fields (for AzTEC Lockman Hole versus AzTEC UDS $p = 16$ per cent, while for SCUBA Lockman Hole versus SCUBA UDS $p = 14$ per cent). This difference starts to become statistically significant if we combine the AzTEC and SCUBA samples in each field (i.e. if for each field we construct a combined catalogue containing both AzTEC and SCUBA sources in that field), and then repeat the redshift distribution comparison. This yields a probability that the
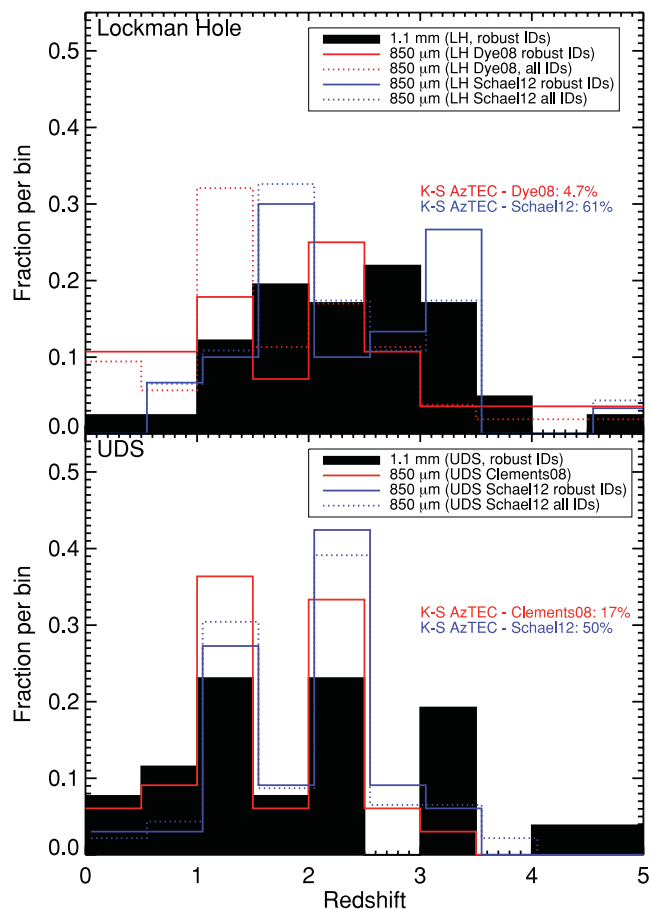
redshift distributions of the combined (AzTEC+SCUBA) Lockman Hole and UDS samples are drawn from the same population of only 2 per cent (a statistical difference between the AzTEC source population in the Lockman Hole and UDS fields was also noted by Austermann et al. 2010, who showed that the 1.1 mm number counts at high fluxes in the Lockman Hole field are higher than in the UDS field; see their fig. 8 as well as the top panel of Fig. 1 in this paper).

This result suggests that the large-scale structures traced by the AzTEC survey are significantly different between the Lockman Hole and UDS fields, and the AzTEC and SCUBA SMG samples are tracing *the same* large-scale structures within each field. This latter result implies that these structures extend from the $\simeq 0\overset{.}{.}3$ areas sampled by the SCUBA to at least the $\simeq 0\overset{.}{.}7$ scales traced by each AzTEC-SHADES survey field. These angular scales correspond to
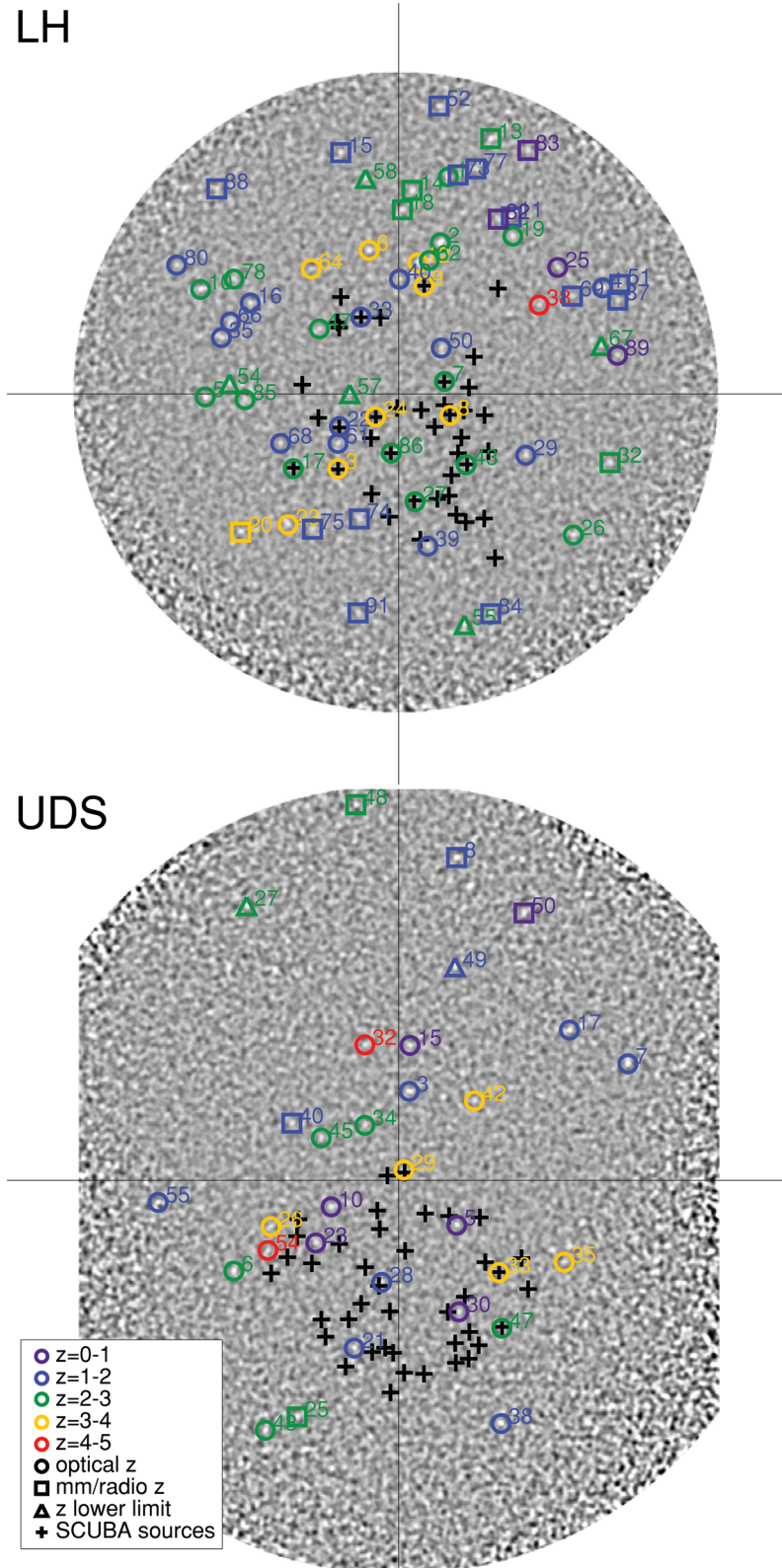
Figure 7. The same as Fig. 4, but this time only showing robust (category 1) IDs.

10–20 Mpc at $z = 1.25$ and 2.25 (the redshifts of the prominent peaks seen in the redshift distribution of the UDS SMGs). Alternatively, large-scale structures at lower redshifts may also contribute to the appearance of this effect, as Aretxaga et al. (2011) showed that the

clustering of the foreground galaxies at $z \simeq 0.7$ is correlated with the position of bright SMGs in the COSMOS field.

In order to investigate whether large-scale structure is in fact expected to produce the variations we see between the Lockman

Hole and UDS fields, we have analysed a $900\,\mathrm{deg}^2$ light cone of simulated galaxies at $z = 0\text{–}5$ with SFR $> 100\,\mathrm{M}_\odot\,\mathrm{yr}^{-1}$ (Croton et al. 2006),[5] produced in a semi-analytic model based on the Millennium simulation (Springel et al. 2005). Interestingly, to match the AzTEC number counts and produce a redshift distribution which peaks at $z \sim 2\text{–}3$ rather than rising monotonically out to $z > 5$, we had to apply a stellar mass cut to the simulation to confine our analysis to galaxies with $M_* > 10^{11}\,\mathrm{M}_\odot$. Confining our attention to this high-mass regime, we then randomly chose $1000\,0.35\,\mathrm{deg}^2$ fields from within this light cone and, for each pair of fields, calculated the KS probability that the galaxy redshift distributions are drawn from the same population. We found that $\simeq 10$ per cent of field pairs were inconsistent at a KS probability level of <5 per cent and that $\simeq 25$ per cent of pairs were inconsistent at a probability level <15 per cent. Hence, the level of inconsistency we found between the Lockman Hole and the UDS AzTEC source populations is broadly as predicted by the simulation, providing some support for the interpretation that it is indeed due to large-scale structures.

For illustrative purposes, Fig. 8 shows the redshift distributions of the random fields which yielded the highest KS probability of being consistent with the Lockman Hole and UDS fields (99 and 14 per cent, respectively). Thus, the light cones produced using this particular simulation can certainly yield SMG number densities and redshift distributions consistent with those seen in both AzTEC-SHADES fields. However, it is clear that the SMG redshift distribution in the Lockman Hole field is much more typical of what is found within the simulations than is the redshift distribution in the UDS field. Specifically, $\simeq 70$ per cent of the simulated $0.35\,\mathrm{deg}^2$ AzTEC surveys yield a KS probability >5 per cent that their SMG redshift distribution is consistent with that of the AzTEC sources in the Lockman Hole field, but this is true for only $\simeq 1$ per cent of the simulated fields when compared to the UDS SMG redshift distribution. Thus, *for this particular simulation* it would appear the observed redshift distribution in the UDS field is relatively unusual, albeit not unfeasibly so.

Our analysis of this simulation also indicates that it is unsurprising that the redshift distributions of the SHADES-SCUBA and SHADES-AzTEC sources within a given field should be in good agreement (Fig. 6), as the overlapping $1.1\,\mathrm{mm}$ and $850\,\mathrm{\mu m}$ surveys, while differing in size, wavelength and depth, are tracing the same large-scale structures (see Fig. 8). Namely, virtually all random $0.35\,\mathrm{deg}^2$ fields have the KS probability above 5 per cent that their redshift distribution is consistent with that of overlapping $0.1\,\mathrm{deg}^2$ fields.

Finally we note that the fact the two well-separated SHADES fields, despite each covering $\simeq 0.35\,\mathrm{deg}^2$, still yield significantly different redshift SMG distributions serves to reinforce the importance of completing SMG surveys over several deg^2 in order to overcome cosmic variance and obtain a complete and representative view of the number density, redshift distribution and evolution of SMGs in the context of the general high-redshift galaxy population.

8 CONCLUSIONS

We have used the deep optical-to-radio multiwavelength data in the SHADES Lockman Hole East and SXDF/UDS fields to obtain galaxy IDs for $\simeq 64$ per cent ($\simeq 80$ per cent including tentative IDs) of the 148 AzTEC-SHADES $1.1\,\mathrm{mm}$ sources reported by Austermann et al. (2010), exploiting deep radio and $24\,\mathrm{\mu m}$ data comple-

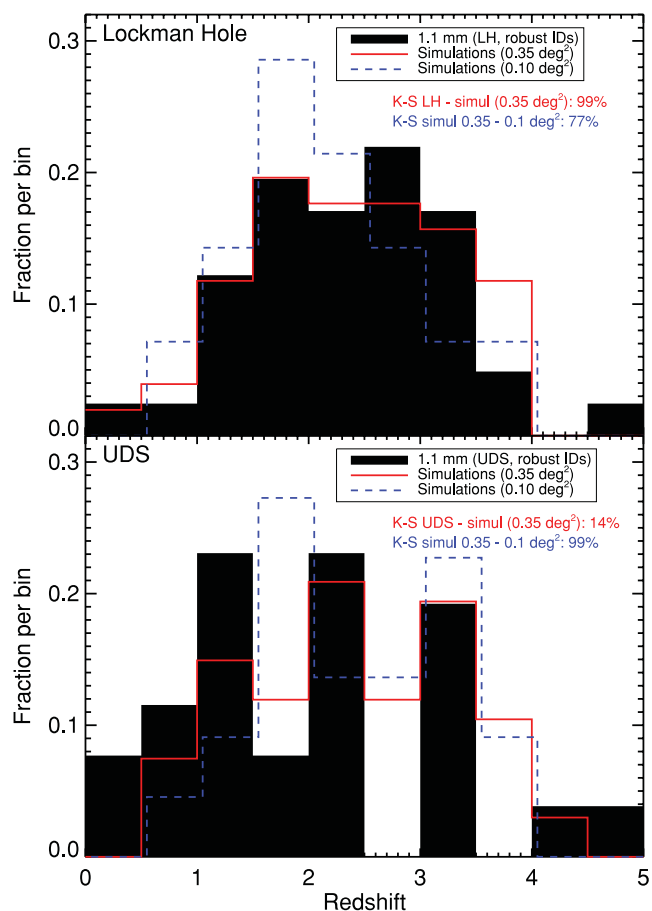[5] http://tao.it.swin.edu.au/mock-galaxy-factory/

Figure 8. The redshift distribution of 1.1-mm-selected galaxies in the Lockman Hole (upper panel) and the UDS (lower panel) fields with robust ($p < 0.05$) IDs and optical–near-IR or 1.1 mm-to-1.4 GHz flux density ratio redshifts (solid black histograms). Sources with only lower limits to their estimated redshifts were excluded. Also shown in this figure are the redshift distributions of simulated galaxies (Croton et al. 2006) in random 0.35 (AzTEC like, red solid lines) and $0.1\,\mathrm{deg}^{-2}$ (SCUBA like, blue dotted lines) fields. For each panel, these simulated fields were chosen out of 1000 random fields to best represent the distributions of real SMGs. The KS test probabilities that the real and simulated galaxies (as well as simulated galaxies in fields with different sizes) in each panel are drawn from the same populations are indicated.

mented by methods based on $8\,\mathrm{\mu m}$ flux density and red optical–IR ($i - K$) colour. This unusually high ID rate can be attributed to the relatively bright mm-wavelength flux density threshold, combined with the relatively deep supporting multifrequency data now available in these two well-studied fields. We have further exploited the optical–mid-IR–radio data to derive an $\simeq 60$ per cent ($\simeq 75$ per cent including tentative IDs) complete redshift distribution for the AzTEC-SHADES sources, yielding a median redshift of $z \simeq 2.2$, with a high-redshift tail extending to at least $z \simeq 4$.

Despite the larger area probed by the AzTEC survey relative to the original SCUBA SHADES imaging, the redshift distribution of the AzTEC sources is consistent with that displayed by the SCUBA sources, and reinforces tentative evidence that the redshift distribution of mm/submm sources in the Lockman Hole field is significantly different from that found in the SXDF/UDS field. Comparison with simulated surveys of similar scale extracted from semi-analytic models based on the Millennium simulation indicates that this is as expected if the mm/submm sources are massive ($M > 10^{11}\,\mathrm{M}_\odot$) star-forming galaxies tracing large-scale structures

over scales of 10–20 Mpc. This confirms the importance of surveys covering several square degrees (as now underway with SCUBA2) to obtain representative samples of bright (sub)mm-selected galaxies.

ACKNOWLEDGMENTS

REFERENCES

Amblard A. et al., 2010, A&A, 518, L9
Aretxaga I., Hughes D. H., Chapin E. L., Gaztañaga E., Dunlop J. S., Ivison R. J., 2003, MNRAS, 342, 759
Aretxaga I. et al., 2007, MNRAS, 379, 1571
Aretxaga I. et al., 2011, MNRAS, 415, 3831
Ashby M. L. N. et al., 2006, ApJ, 644, 778
Austermann J. E. et al., 2009, MNRAS, 393, 1573
Austermann J. E. et al., 2010, MNRAS, 401, 160
Barger A. J., Cowie L. L., Sanders D. B., Fulton E., Taniguchi Y., Sato Y., Kawara K., Okuda H., 1998, Nat, 394, 248
Barger A. J., Cowie L. L., Sanders D. B., 1999, ApJ, 518, L5
Barger A. J., Cowie L. L., Richards E. A., 2000, AJ, 119, 2092
Barger A. J., Cowie L. L., Steffen A. T., Hornschemeier A. E., Brandt W. N., Garmire G. P., 2001, ApJ, 560, L23
Barger A. J., Cowie L. L., Brandt W. N., Capak P., Garmire G. P., Hornschemeier A. E., Steffen A. T., Wehner E. H., 2002, AJ, 124, 1839
Bertin E., Arnouts S., 1996, A&AS, 117, 393
Bertoldi F. et al., 2007, ApJS, 172, 132
Béthermin M. et al., 2012, A&A, 542, A58
Biggs A. D. et al., 2011, MNRAS, 413, 2314
Bolzonella M., Miralles J., Pelló R., 2000, A&A, 363, 476
Borys C., Smail I., Chapman S. C., Blain A. W., Alexander D. M., Ivison R. J., 2005, ApJ, 635, 853
Bruzual G., Charlot S., 2003, MNRAS, 344, 1000
Bussmann R. S. et al., 2012, ApJ, 744, 150
Calzetti D., Armus L., Bohlin R. C., Kinney A. L., Koornneef J., Storchi-Bergmann T., 2000, ApJ, 533, 682
Capak P. et al., 2008, ApJ, 681, L53
Capak P. L. et al., 2011, Nat, 470, 233
Caputi K. I., Dole H., Lagache G., McLure R. J., Dunlop J. S., Puget J., Le Floc'h E., Pérez-González P. G., 2006, A&A, 454, 143
Caputi K. I., Cirasuolo M., Dunlop J. S., McLure R. J., Farrah D., Almaini O., 2011, MNRAS, 413, 162
Chabrier G., 2003, ApJ, 586, L133
Chapin E. L. et al., 2009, MNRAS, 398, 1793
Chapin E. L. et al., 2011, MNRAS, 411, 505
Chapman S. C., Richards E. A., Lewis G. F., Wilson G., Barger A. J., 2001, ApJ, 548, L147
Chapman S. C. et al., 2003, ApJ, 585, 57
Chapman S. C., Blain A. W., Smail I., Ivison R. J., 2005, ApJ, 622, 772
Cirasuolo M. et al., 2007, MNRAS, 380, 585
Cirasuolo M., McLure R. J., Dunlop J. S., Almaini O., Foucaud S., Simpson C., 2010, MNRAS, 401, 1166
Clements D. L. et al., 2008, MNRAS, 387, 247
Combes F. et al., 2012, A&A, 538, L4
Condon J. J., 1992, ARA&A, 30, 575
Coppin K., Halpern M., Scott D., Borys C., Chapman S., 2005, MNRAS, 357, 1022
Coppin K. et al., 2006, MNRAS, 372, 1621
Coppin K. et al., 2008, MNRAS, 384, 1597
Coppin K. E. K. et al., 2009, MNRAS, 395, 1905
Coppin K. et al., 2010, ApJ, 713, 503
Cox P. et al., 2011, ApJ, 740, 63
Croton D. J. et al., 2006, MNRAS, 365, 11
Daddi E., Dannerbauer H., Krips M., Walter F., Dickinson M., Elbaz D., Morrison G. E., 2009a, ApJ, 695, L176
Daddi E. et al., 2009b, ApJ, 694, 1517
Dannerbauer H., Lehnert M. D., Lutz D., Tacconi L., Bertoldi F., Carilli C., Genzel R., Menten K. M., 2004, ApJ, 606, 664
Dannerbauer H. et al., 2010, ApJ, 720, L144
Downes A. J. B., Peacock J. A., Savage A., Carrie D. R., 1986, MNRAS, 218, 31
Downes T. P., Welch D., Scott K. S., Austermann J., Wilson G. W., Yun M. S., 2012, MNRAS, 423, 529
Dunlop J. S., Peacock J. A., Savage A., Lilly S. J., Heasley J. N., Simon A. J. B., 1989, MNRAS, 238, 1171
Dunlop J. S. et al., 2004, MNRAS, 350, 769
Dunlop J. S. et al., 2010, MNRAS, 408, 2022
Dye S. et al., 2006, MNRAS, 372, 1227
Dye S. et al., 2008, MNRAS, 386, 1107
Eales S. et al., 2009, ApJ, 707, 1779
Egami E. et al., 2004, ApJS, 154, 130
Engel H. et al., 2010, ApJ, 724, 233
Ezawa H., Kawabe R., Kohno K., Yamamoto S., 2004, in Oschmann J. M., Jr, ed., SPIE Conf. Ser. Vol. 5489, Ground-based Telescopes. SPIE, Bellingham, p. 763
Ezawa H. et al., 2008, in Stepp L. M., Gilmozzi R., eds, SPIE Conf. Ser. Vol. 7012, Ground-based and Airborne Telescopes II. SPIE, Bellingham, p. 701208
Furusawa H. et al., 2008, ApJS, 176, 1
Greve T. R., Ivison R. J., Bertoldi F., Stevens J. A., Dunlop J. S., Lutz D., Carilli C. L., 2004, MNRAS, 354, 779
Greve T. R. et al., 2005, MNRAS, 359, 1165
Greve T. R., Pope A., Scott D., Ivison R. J., Borys C., Conselice C. J., Bertoldi F., 2008, MNRAS, 389, 1489
Hainline L. J., Blain A. W., Smail I., Frayer D. T., Chapman S. C., Ivison R. J., Alexander D. M., 2009, ApJ, 699, 1610
Hainline L. J., Blain A. W., Smail I., Alexander D. M., Armus L., Chapman S. C., Ivison R. J., 2011, ApJ, 740, 96
Hatsukade B. et al., 2010, ApJ, 711, 974
Hatsukade B. et al., 2011, MNRAS, 411, 102
Hayward C. C., Kereš D., Jonsson P., Narayanan D., Cox T. J., Hernquist L., 2011, ApJ, 743, 159
Holland W. S. et al., 1999, MNRAS, 303, 659
Hughes D. H. et al., 1998, Nat, 394, 241
Ibar E., Ivison R. J., Biggs A. D., Lal D. V., Best P. N., Green D. A., 2009, MNRAS, 397, 281
Ibar E., Ivison R. J., Best P. N., Coppin K., Pope A., Smail I., Dunlop J. S., 2010, MNRAS, 401, L53

Ivison R. J. et al., 2002, MNRAS, 337, 1

Ivison R. J. et al., 2005, MNRAS, 364, 1025

Ivison R. J. et al., 2007, MNRAS, 380, 199

Joye W. A., Mandel E., 2003, in Payne H. E., Jedrzejewski R. I., Hook R. N., eds, ASP Conf. Ser. Vol. 295, Astronomical Data Analysis Software and Systems XII. Astron. Soc. Pac., San Francisco, p. 489

Knudsen K. K., Kneib J. P., Egami E., 2008, in Chary R. R., Teplitz H. I., Sheth K., eds, ASP Conf. Ser. Vol. 381, Infrared Diagnostics of Galaxy Evolution. Astron. Soc. Pac., San Francisco, p. 372

Knudsen K. K., Kneib J., Richard J., Petitpas G., Egami E., 2010, ApJ, 709, 210

Lawrence A. et al., 2007, MNRAS, 379, 1599

Lindner R. R. et al., 2011, ApJ, 737, 83

McLure R. J., Cirasuolo M., Dunlop J. S., Foucaud S., Almaini O., 2009, MNRAS, 395, 2196

Madau P., 1995, ApJ, 441, 18

Marsden G. et al., 2011, MNRAS, 417, 1192

Michałowski M., Hjorth J., Watson D., 2010a, A&A, 514, A67

Michałowski M. J., Watson D., Hjorth J., 2010b, ApJ, 712, 942

Michałowski M. J., Dunlop J. S., Cirasuolo M., Hjorth J., Hayward C. C., Watson D., 2012, A&A, 541, A85

Miyazaki S. et al., 2002, PASJ, 54, 833

Mortier A. M. J. et al., 2005, MNRAS, 363, 563

Negrello M. et al., 2010, Sci, 330, 800

Perera T. A. et al., 2008, MNRAS, 391, 1227

Pope A. et al., 2006, MNRAS, 370, 1185

Riechers D. A. et al., 2010, ApJ, 720, L131

Santini P. et al., 2010, A&A, 518, L154

Schael A. M., 2009, PhD thesis, Univ. Edinburgh

Schinnerer E. et al., 2008, ApJ, 689, L5

Scott S. E. et al., 2002, MNRAS, 331, 817

Scott K. S. et al., 2008, MNRAS, 385, 2225

Scott K. S. et al., 2010, MNRAS, 405, 2260

Scott K. S. et al., 2012, MNRAS, 423, 575

Serjeant S. et al., 2008, MNRAS, 386, 1907

Shang Z. et al., 2011, ApJS, 196, 2

Shimizu I., Yoshida N., Okamoto T., 2012, MNRAS, preprint (arXiv:1207.3856)

Silva L., Granato G. L., Bressan A., Danese L., 1998, ApJ, 509, 103

Siringo G. et al., 2009, A&A, 497, 945

Smail I., Ivison R. J., Blain A. W., 1997, ApJ, 490, L5

Smail I., Ivison R. J., Kneib J. P., Cowie L. L., Blain A. W., Barger A. J., Owen F. N., Morrison G., 1999, MNRAS, 308, 1061

Smail I., Ivison R. J., Blain A. W., Kneib J. P., 2002, MNRAS, 331, 495

Smail I., Chapman S. C., Blain A. W., Ivison R. J., 2004, ApJ, 616, 71

Smolčić V. et al., 2011, ApJ, 731, L27

Springel V. et al., 2005, Nat, 435, 629

Swinbank A. M., Smail I., Chapman S. C., Blain A. W., Ivison R. J., Keel W. C., 2004, ApJ, 617, 64

Swinbank A. M., Chapman S. C., Smail I., Lindner C., Borys C., Blain A. W., Ivison R. J., Lewis G. F., 2006, MNRAS, 371, 465

Tacconi L. J. et al., 2006, ApJ, 640, 228

Tacconi L. J. et al., 2008, ApJ, 680, 246

Takagi T., Hanami H., Arimoto N., 2004, MNRAS, 355, 424

Takagi T. et al., 2007, MNRAS, 381, 1154

Targett T. A., Dunlop J. S., McLure R. J., Best P. N., Cirasuolo M., Almaini O., 2011, MNRAS, 412, 295

Targett T. A. et al., 2012, MNRAS, preprint (arXiv:1208.3464)

Taylor M. B., 2005, in Shopbell P., Britton M., Ebert R., eds, ASP Conf. Ser. Vol. 347, Astronomical Data Analysis Software and Systems XIV. Astron. Soc. Pac., San Francisco, p. 29

van Kampen E. et al., 2005, MNRAS, 359, 469

Vega O., Clemens M. S., Bressan A., Granato G. L., Silva L., Panuzzo P., 2008, A&A, 484, 631

Vieira J. D. et al., 2010, ApJ, 719, 763

Wagg J., Owen F., Bertoldi F., Sawitzki M., Carilli C. L., Menten K. M., Voss H., 2009, ApJ, 699, 1843

Wall J. V., Pope A., Scott D., 2008, MNRAS, 383, 435

Walter F. et al., 2012, Nat, 286, 233

Wang W. H., Cowie L. L., Barger A. J., 2004, ApJ, 613, 655

Wang W. H., Cowie L. L., Barger A. J., Williams J. P., 2011, ApJ, 726, L18

Wardlow J. L. et al., 2011, MNRAS, 415, 1479

Warren S. J. et al., 2007, MNRAS, 375, 213

Webb T. M. A., Lilly S. J., Clements D. L., Eales S., Yun M., Brodwin M., Dunne L., Gear W. K., 2003, ApJ, 597, 680

Weiß A. et al., 2009, ApJ, 707, 1201

Wilson G. W. et al., 2008, MNRAS, 386, 807

Younger J. D. et al., 2008, MNRAS, 387, 707

Yun M. S. et al., 2012, MNRAS, 420, 957

APPENDIX A: NOTES ON INDIVIDUAL SOURCES

AzLOCK1: A robust single ID (category 1). The spectroscopic mid-IR PAH redshift from Coppin et al. (2010) was adopted.

AzLOCK2: A robust single ID (category 1).

AzLOCK3: This source has two category 1 radio IDs, but the high-resolution submm imaging obtained by Younger et al. (2008) revealed that the first one (the northern, 24 μm faint ID) is the correct ID. This is the SCUBA source LOCK850.02 (Ivison et al. 2007). The same IDs were selected.

AzLOCK4: Three candidate category 1 radio IDs. The one with the lowest *p* value, and confirmation at low radio frequency and 24 μm was adopted.

AzLOCK5: A robust single ID (category 1). A possible blend of weak 24 μm sources. The spectroscopic mid-IR PAH redshift from Coppin et al. (2010) was adopted.

AzLOCK6: A robust single radio and 8 μm ID (category 1).

AzLOCK7: A possible blend of two radio/24 μm sources and an additional red $i - K$ source (category 1) at the same redshift as the first ID. This is the SCUBA source LOCK850.04 (Ivison et al. 2007). The faintest radio ID considered by Ivison et al. (2007) is not in the catalogue used here, as it is blended with the brighter object. The spectroscopic redshift from Ivison et al. (2007) was adopted for the second ID, but the first ID is the one adopted here.

AzLOCK8: A robust single ID (category 1). This is the SCUBA source LOCK850.01 (Ivison et al. 2007). The same ID was selected. The spectroscopic mid-IR PAH redshift from Coppin et al. (2010) was adopted.

AzLOCK9: A robust ID (category 1) with two possible weaker IDs (category 3). This is the SCUBA source LOCK850.34 (Ivison et al. 2007). We did not select their fainter radio counterpart due to its low significance and we also considered one additional 24 μm candidate.

AzLOCK10: A robust ID (category 1) with a possible weaker ID (category 3). The spectroscopic mid-IR PAH redshift from Coppin et al. (2010) was adopted for the robust ID.

AzLOCK11: A robust ID (category 1) with a possible radio companion (category 1).

AzLOCK12: A robust ID (category 1) with a possible radio companion (category 3).

AzLOCK13: A robust single ID (category 1).

AzLOCK14: A robust single ID (category 1).

AzLOCK15: A robust single ID (category 1).

AzLOCK16: A robust single ID (category 1) with a possible 8.0 μm companion (category 3). A possible blend of weak 24 μm sources.

AzLOCK17: A robust single ID (category 1). A possible blend of weak 24 μm sources. This is the SCUBA source LOCK850.15 (Ivison et al. 2007). We selected only their second radio IDs as the remaining two are too far away from the AzTEC position.

AzLOCK18: A robust single ID (category 1).

AzLOCK19: A robust ID (category 1) with a possible red $i - K$ companion (category 3). A possible blend of weak 24 μm sources.

AzLOCK20: Two robust IDs (category 1) with a possible weaker radio companion (category 3). A possible blend of weak 24 μm sources.

AzLOCK21: A single ID (category 2). A possible blend of weak 24 μm sources. This is the SCUBA source LOCK850.13 (Ivison et al. 2007). We only selected the brighter (southern) out of their two 24 μm IDs, because of low significance of the other one.

AzLOCK22: A blend of four radio sources (category 1 and 3). This is the SCUBA source LOCK850.43 (Ivison et al. 2007). We selected two out of three of their radio IDs and selected two additional IDs. The inconsistency can be explained by the fact that the radio image is severely blended at this position.

AzLOCK23: A robust single ID (category 1) with a possible weaker red $i - K$ companion (category 3).

AzLOCK24: A blend of three radio sources (category 1 and 2). This is the SCUBA source LOCK850.03 (Ivison et al. 2007). We selected both of their radio IDs and an additional faint radio ID. The spectroscopic redshift from Ivison et al. (2007) was adopted.

AzLOCK25: A robust ID (category 1) with a possible radio companion (category 3).

AzLOCK26: A robust single ID (category 1).

AzLOCK27: Three robust IDs (category 1). A possible blend of weak 24 μm sources. This is the SCUBA source LOCK850.71 (Ivison et al. 2007). The same IDs were selected.

AzLOCK28: No IDs obtained (but only the radio selection could yield IDs due to lack of coverage at other wavelengths).

AzLOCK29: A robust single ID (category 1).

AzLOCK30: No IDs obtained.

AzLOCK31: No IDs obtained. A possible blend of weak 24 μm sources.

AzLOCK32: A robust single ID (category 1). A possible blend of weak 24 μm sources.

AzLOCK33: Two robust IDs (category 1). This is the SCUBA source LOCK850.52 (Ivison et al. 2007). The same ID was selected.

AzLOCK34: No IDs obtained.

AzLOCK35: Three IDs (category 1 and 3).

AzLOCK36: A single ID (category 2).

AzLOCK37: Three IDs (category 2 and 3).

AzLOCK38: A robust single ID (category 1).

AzLOCK39: Three IDs (category 1 and 3). A possible blend of weak 24 μm sources.

AzLOCK40: Three IDs (category 1 and 3).

AzLOCK41: A single ID (category 2). A possible blend of weak 24 μm sources.

AzLOCK42: No IDs obtained. A possible blend of weak 24 μm sources.

AzLOCK43: Three IDs (category 1 and 3). A possible blend of weak 24 μm sources. This is the SCUBA source LOCK850.79 (Ivison et al. 2007). We selected the same IDs.

AzLOCK44: A tentative single ID (category 3). A possible blend of weak 24 μm sources.

AzLOCK45: A single ID (category 2). A possible blend of weak 24 μm sources.

AzLOCK46: No IDs obtained. A possible blend of weak 24 μm sources.

AzLOCK47: A robust single ID (category 1).

AzLOCK48: No IDs obtained (but the 8.0 μm and $i - K$ methods could not be used due to lack of coverage at these wavelengths).

AzLOCK49: No IDs obtained.

AzLOCK50: A robust single ID (category 1). A possible blend of weak 24 μm sources.

AzLOCK51: Three IDs (category 1 and 3).

AzLOCK52: A robust single ID (category 1).

AzLOCK53: No IDs obtained.

AzLOCK54: Four IDs (category 1, 2 and 3).

AzLOCK55: Three IDs (category 1 and 3).

AzLOCK56: Three IDs (category 2). This is the SCUBA source LOCK850.06 (Ivison et al. 2007). The same IDs were selected.

AzLOCK57: A single ID (category 1). A possible blend of weak 24 μm sources.

AzLOCK58: Two IDs (category 1).

AzLOCK59: No IDs obtained (but the 8.0 μm and $i - K$ methods could not be used due to lack of coverage at these wavelengths).

AzLOCK60: No IDs obtained. A possible blend of weak 24 μm sources.

AzLOCK61: Two IDs (category 1 and 3). A possible blend of weak 24 μm sources.

AzLOCK62: A robust single ID (category 1). The spectroscopic mid-IR PAH redshift from Coppin et al. (2010) was adopted.

AzLOCK63: Two IDs (category 2 and 3).

AzLOCK64: A robust single ID (category 1). A possible blend of weak 24 μm sources.

AzLOCK65: A tentative single ID (category 3). A possible blend of weak 24 μm sources.

AzLOCK66: A robust single ID (category 1). A possible blend of weak 24 μm sources.

AzLOCK67: Two IDs (category 1 and 3).

AzLOCK68: A robust single ID (category 1). A possible blend of weak 24 μm sources.

AzLOCK69: A robust single ID (category 1).

AzLOCK70: No IDs obtained. A possible blend of weak 24 μm sources.

AzLOCK71: A tentative single ID (category 3).

AzLOCK72: A tentative single ID (category 3). A possible blend of weak 24 μm sources.

AzLOCK73: A robust single ID (category 1).

AzLOCK74: Two IDs (category 1 and 3). A possible blend of weak 24 μm sources.

AzLOCK75: Two IDs (category 1 and 3). A possible blend of weak 24 μm sources.

AzLOCK76: A tentative single ID (category 3). A possible blend of weak 24 μm sources.

AzLOCK77: Two IDs (category 1 and 3). A possible blend of weak 24 μm sources.

AzLOCK78: A robust single ID (category 1). A possible blend of weak 24 μm sources.

AzLOCK79: A tentative single ID (category 3). A possible blend of weak 24 μm sources.

AzLOCK80: Two IDs (category 1) at similar redshifts.

AzLOCK81: Two IDs (category 3). A possible blend of weak 24 μm sources.

AzLOCK82: Five IDs (category 1 and 3).

AzLOCK83: A robust single ID (category 1). A possible blend of weak 24 μm sources.

AzLOCK84: A robust single ID (category 1). A possible blend of weak 24 μm sources.

AzLOCK85: Four IDs (category 1 and 2).

AzLOCK86: Three IDs (category 1 and 3). A possible blend of weak 24 μm sources. This is the SCUBA source LOCK850.14 (Ivison et al. 2007). We only selected the closer out of their two radio IDs,

because of low significance of the other one. The spectroscopic redshift from Ivison et al. (2007) was adopted.

AzLOCK87: A robust single ID (category 1).

AzLOCK88: A robust single ID (category 1). A possible blend of weak 24 μm sources.

AzLOCK89: Two robust IDs (category 1) at low redshift (0.14). A possible blend of weak 24 μm sources. Its 1.1 mm-to-1.4 GHz flux density ratio is also consistent with $z \lesssim 0.5$.

AzLOCK90: No IDs obtained.

AzLOCK91: A robust single ID (category 1).

AzUDS1: No IDs obtained (but the 8.0 μm and $i - K$ methods could not be used due to lack of coverage at these wavelengths).

AzUDS2: A tentative single ID (category 3).

AzUDS3: Two robust IDs (category 1).

AzUDS4: No IDs obtained (but the $i - K$ method could not be used due to lack of coverage at these wavelengths). A possible blend of weak 24 μm sources.

AzUDS5: A robust single ID (category 1). This is the SCUBA source SXDF850.03 (Ivison et al. 2007). The same ID was selected. The optical counterpart and the radio ID may correspond to a possible lensing galaxy and a lensed source (see Section 4).

AzUDS6: Two IDs (category 1 and 3).

AzUDS7: Two IDs (category 1 and 3).

AzUDS8: A robust single ID (category 1).

AzUDS9: No IDs obtained. A possible blend of weak 24 μm sources.

AzUDS10: A robust single ID (category 1). A very close star makes the photometry difficult to obtain. This is the SCUBA source SXDF850.29 (Ivison et al. 2007). The same ID was selected.

AzUDS11: A tentative single ID (category 3). A possible blend of weak 24 μm sources.

AzUDS12: A tentative single ID (category 3).

AzUDS13: A tentative single ID (category 3).

AzUDS14: No IDs obtained.

AzUDS15: Two IDs (category 1 and 3).

AzUDS16: A single ID (category 2).

AzUDS17: Two IDs (category 1 and 3).

AzUDS18: No IDs obtained (but the 8 μm and $i - K$ methods could not be used due to lack of coverage at these wavelengths).

AzUDS19: No IDs obtained (but the $i - K$ methods could not be used due to lack of coverage at these wavelengths).

AzUDS20: No IDs obtained.

AzUDS21: Two IDs (category 1 and 3).

AzUDS22: No IDs obtained (but the $i - K$ methods could not be used due to lack of coverage at these wavelengths).

AzUDS23: A robust single ID (category 1).

AzUDS24: No IDs obtained (but the $i - K$ methods could not be used due to lack of coverage at these wavelengths).

AzUDS25: A robust single ID (category 1).

AzUDS26: Two IDs (category 1 and 3).

AzUDS27: Three IDs (category 1 and 3). A possible blend of weak 24 μm sources.

AzUDS28: Two IDs (category 1 and 3) at similar redshifts. A possible blend of weak 24 μm sources.

AzUDS29: Two IDs (category 1 and 3). A possible blend of weak 24 μm sources.

AzUDS30: Two IDs (category 1 and 3). A possible blend of weak 24 μm sources.

AzUDS31: No IDs obtained.

AzUDS32: A robust single ID (category 1).

AzUDS33: Two IDs (category 1 and 3). This is the SCUBA source SXDF850.01 (Ivison et al. 2007). We selected an additional category 3 ID.

AzUDS34: A robust single ID (category 1).

AzUDS35: A robust single ID (category 1).

AzUDS36: A single ID (category 3).

AzUDS37: No IDs obtained.

AzUDS38: Five IDs (category 1 and 3). A possible blend of weak 24 μm sources.

AzUDS39: No IDs obtained. A possible blend of weak 24 μm sources.

AzUDS40: Two IDs (category 1 and 3).

AzUDS41: No IDs obtained.

AzUDS42: Five IDs (category 1 and 3). A possible blend of weak 24 μm sources.

AzUDS43: Two robust IDs (category 1). A possible blend of weak 24 μm sources. The first and second IDs may correspond to a possible lensing galaxy and a lensed source (see Section 4). The redshift of the second ID was used in the analysis of the redshift distribution.

AzUDS44: No IDs obtained.

AzUDS45: A robust single ID (category 1). A possible blend of weak 24 μm sources.

AzUDS46: No IDs obtained.

AzUDS47: Five IDs (category 1). The high-resolution submm imaging revealed that the second one (the most northern with $z \simeq 2.48$) is the correct ID (Hatsukade et al. 2010). This is the SCUBA source SXDF850.06 (Ivison et al. 2007). The same radio IDs were selected.

AzUDS48: A robust single ID (category 1). A possible blend of weak 24 μm sources.

AzUDS49: A robust single ID (category 1).

AzUDS50: Two IDs (category 1 and 3). A possible blend of weak 24 μm sources.

AzUDS51: No IDs obtained. This is the SCUBA source SXDF850.5 (Ivison et al. 2007). Their 3σ radio ID is not selected as it is too far away from the AzTEC position, which is offset from the SCUBA position by $\simeq 5$ arcsec.

AzUDS52: Four tentative IDs (category 3).

AzUDS53: A tentative ID (category 3).

AzUDS54: A robust single ID (category 1).

AzUDS55: A robust single ID (category 1). A possible blend of weak 24 μm sources.

AzUDS56: No IDs obtained. A possible blend of weak 24 μm sources. This is the SCUBA source SXDF850.18 (Ivison et al. 2007). Their radio ID was not selected due to its low significance.

AzUDS57: A tentative single ID (category 3).

APPENDIX B: FIGURES AND TABLES
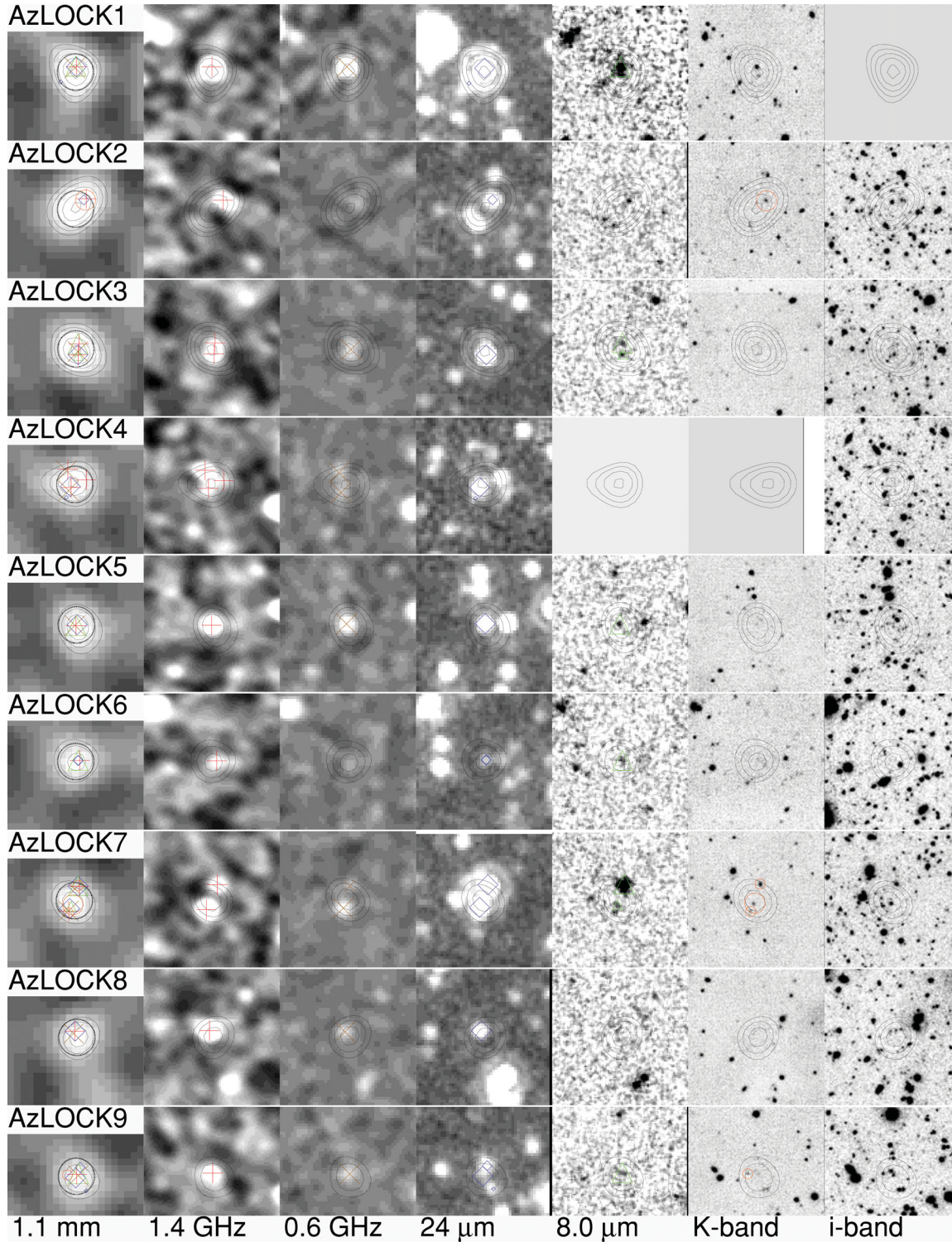
Figure B1. Thumbnail images of AzTEC sources in the Lockman Hole field. Each panel is 60 arcsec on a side and centred on the AzTEC position. From the left-hand to right-hand side: 1.1 mm, 1.4 GHz, 0.61 GHz, 24 μm, 8.0 μm, K band and i band. The IDs are marked on the relevant images: red pluses – 1.4 GHz IDs; blue diamonds – 24 μm IDs; brown crosses – 0.61 GHz IDs; green triangles – 8.0 μm IDs; orange circles – $i - K > 2$. Big symbols: reliable IDs ($p < 0.05$), medium symbols: tentative IDs ($0.05 < p < 0.1$), small symbols: bad IDs ($p > 0.1$). On the 1.1 mm images all the ID symbols as well as a thick circle corresponding to the search radius (Section 3) are shown. The contours represent 1.1 mm flux and start at 3 mJy with a 1 mJy increment. The rest of the images are available as Supporting Information with the electronic version of the article.
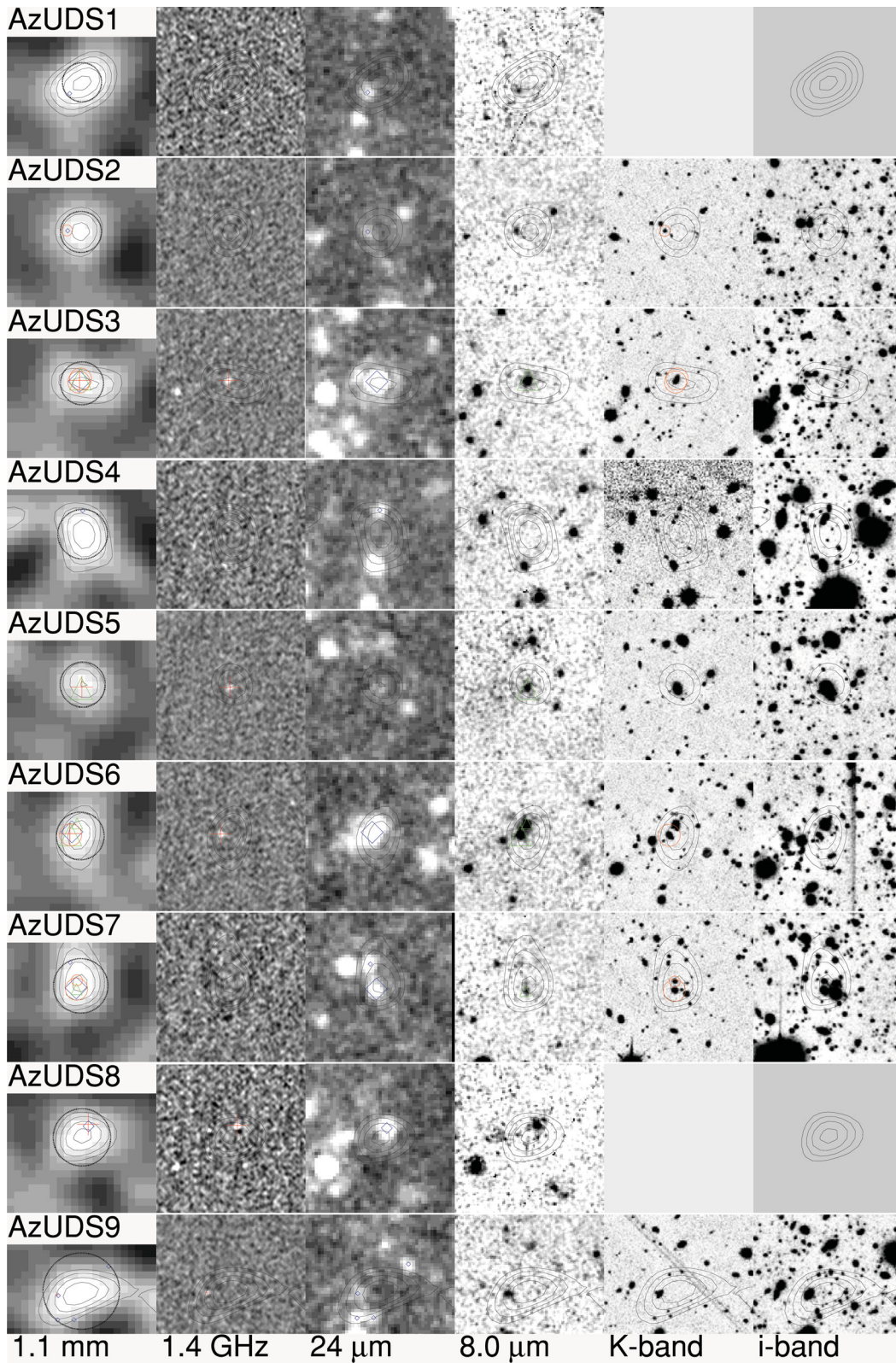
Figure B2. Thumbnail images of AzTEC sources in the UDS field. Symbols are the same as in Fig. B1. The rest of the images are available as Supporting Information with the electronic version of the article.

Table B1. Reliable and tentative radio, 24 μm, 8.0 μm and $i - K$ IDs in the Lockman Hole field. $S_{1.1\,\mu m}$ is deboosted mm flux from Austermann et al. (2010). The coordinates and the distances to the AzTEC sources are that of the 1.4 GHz ID if present and 24 μm (or 0.61 GHz) otherwise. The probabilities of a counterpart to be a chance superposition, p, are bold if $p < 0.05$ and italic if $0.05 < p < 0.1$. In the last column, the photometric redshifts based on optical–near-IR photometry are given. Optical spectroscopic redshifts from Ivison et al. (2007) are shown with no errors and with three significant digits. Mid-IR spectroscopic redshifts from Coppin et al. (2010a) are shown with symmetric errors. Italicized redshifts were calculated from the 1.1 mm-to-1.4 GHz flux density ratio using the average SMG SED from Michałowski et al. (2010a). Bold redshifts indicate an ID used for redshift histogram analysis. N/A is given if an object is not covered by the IRAC map (column $S_{8.0}$ and $p_{8.0}$) or by the i- or K-band map (column $i - K$ and p_{i-K}). Moreover, N/A is given for p values if $S_{8.0} < 20\,\mu$Jy, or $i - K < 2$ or the object is not detected at the K band as such objects were not taken into account for the calculations of p values. Dots represent a non-detection at 8.0 μm (column $S_{8.0}$) and a non-detection at both i and K bands (column $i - K$). This table is available in its entirety in a machine-readable form as Supporting Information with the electronic version of the article. A portion is shown here for guidance regarding its form and content.

No.	$S_{1.1\,\mu m}$ (mJy)	$RA_{\rm ID}$ (°)	$Dec_{\rm ID}$ (°)	Distance (arcsec)	$S_{1.4}$ (μJy)	$p_{1.4}$	$S_{0.6}$ (μJy)	$p_{0.6}$	S_{24} (μJy)	p_{24}	$S_{8.0}$ (μJy)	$p_{8.0}$	K (mag)	$i - K$ (mag)	p_{i-K}	z
1	$6.63^{+0.85}_{-0.97}$	163.008040	57.681007	2.3	258 ± 11	**0.002**	596 ± 24	**0.001**	1642 ± 11	**0.002**	215 ± 19	**0.009**	N/A	N/A	N/A	$\mathbf{2.50 \pm 0.02}$
2	$6.43^{+0.90}_{-0.89}$	163.022900	57.607548	6.5	66 ± 8	**0.038**	...	...	235 ± 6	*0.070*	31 ± 3	0.136	21.7	3.3	0.035	$\mathbf{2.25^{+0.13}_{-0.13}}$
3	$6.21^{+1.05}_{-0.92}$	163.237710	57.350926	2.8	67 ± 7	**0.011**	149 ± 16	**0.004**	636 ± 13	**0.008**	28 ± 2	*0.069*	23.2	<2.0	...	$2.58^{+0.12}_{-0.23}$
...	...	163.237530	57.352273	2.6	36 ± 7	**0.019**	...	...	...	...	30 ± 3	**0.045**	24.1	<2.9	...	$\mathbf{3.07^{+0.11}_{-0.64}}$
4	$5.27^{+0.91}_{-0.97}$	162.686880	57.556959	7.4	150 ± 12	**0.021**	121 ± 17	**0.045**	...	...	N/A	N/A	N/A	N/A	N/A	$2.43^{+0.10}_{-0.08}$
...	...	162.686160	57.554737	2.1	56 ± 11	**0.009**	99 ± 17	**0.025**	284 ± 13	**0.013**	N/A	N/A	N/A	N/A	N/A	$1.39^{+0.58}_{-0.44}$
...	...	162.682660	57.555667	5.5	43 ± 11	**0.044**	...	...	...	...	N/A	N/A	N/A	N/A	N/A	3.0 ± 0.5

[a]The optical photometric redshift could not be measured because this object is outside the optical map (or close to a bright star).

Table B2. Reliable and tentative radio, 24 μm, 8.0 μm and $i - K$ IDs in the UDS field. Columns are described in Table B1. This table is available in its entirety in a machine-readable form as Supporting Information with the electronic version of the article. A portion is shown here for guidance regarding its form and content.

No.	$S_{1.1\,\mu m}$ (mJy)	$RA_{\rm ID}$ (°)	$Dec_{\rm ID}$ (°)	Distance (arcsec)	$S_{1.4}$ (μJy)	$p_{1.4}$	S_{24} (μJy)	p_{24}	$S_{8.0}$ (μJy)	$p_{8.0}$	K (mag)	$i - K$ (mag)	p_{i-K}	z
1	$5.29^{+1.40}_{-1.68}$	...	...	...	...	...	...	...	N/A	N/A	N/A	N/A	N/A	$> \mathbf{2.9}$[a]
2	$3.99^{+1.10}_{-1.34}$	34.442284	-4.796439	5.7	...	...	77 ± 7	0.199	21 ± 2	0.162	22.8	>3.6	0.084	$\mathbf{2.53^{+0.47}_{-0.28}}$
3	$3.75^{+1.22}_{-1.18}$	34.479333	-4.789667	1.5	113 ± 20	**0.002**	776 ± 11	**0.002**	78 ± 7	**0.014**	21.6	3.8	**0.005**	$\mathbf{1.81^{+0.04}_{-0.06}}$
...	...	34.479412	-4.789859	1.4	...	...	...	...	...	...	21.6	4.6	**0.003**	$3.13^{+0.07}_{-0.10}$
4	$4.39^{+1.67}_{-1.58}$	...	...	...	...	...	...	...	N/A	N/A	N/A	N/A	N/A	$> \mathbf{2.7}$[a]
5	$3.57^{+1.19}_{-1.21}$	34.425542	-4.941028	1.0	89 ± 17	**0.002**	...	...	40 ± 4	**0.022**	19.3	1.3	N/A	$\mathbf{0.45^{+0.05}_{-0.05}}$

[a]The optical photometric redshift could not be measured because this object is outside the optical map (or close to a bright star).

Table B3. All radio and 24 μm IDs in the Lockman Hole field. This table is available in its entirety in a machine-readable form as Supporting Information with the electronic version of the article. A portion is shown here for guidance regarding its form and content.

No.	$S_{1.1\mu m}$ (mJy)	$RA_{1.4}$ (°)	$Dec_{1.4}$ (°)	$S_{1.4}$ (μJy)	Distance (arcsec)	p	RA_{24} (°)	Dec_{24} (°)	S_{24} (μJy)	Distance (arcsec)	p	$RA_{0.61}$ (°)	$Dec_{0.61}$ (°)	$S_{0.61}$ (μJy)	Distance (arcsec)	p
1	$6.63^{+0.85}_{-0.97}$	163.008040	57.681007	258 ± 11	2.3	0.002	163.008072	57.681003	1642 ± 11	2.3	0.002	163.008390	57.680893	596 ± 24	1.9	0.001
...	...	...	...	...	...	...	163.011618	57.679160	123 ± 14	7.8	0.206	...	...	...	...	...
2	$6.43^{+0.90}_{-0.89}$	163.022900	57.607548	66 ± 8	6.5	0.038	163.023461	57.607408	235 ± 6	5.4	0.070	...	...	...	...	...
3	$6.21^{+1.05}_{-0.92}$	163.237710	57.350926	67 ± 7	2.8	0.011	163.237751	57.350931	636 ± 13	2.8	0.008	163.237780	57.351320	149 ± 16	1.5	0.004
...	...	163.237530	57.352273	36 ± 7	2.6	0.019	...	...	...	...	...	...	...	...	...	...

Table B4. All radio and 24 μm IDs in the UDS field. This table is available in its entirety in a machine-readable form as Supporting Information with the electronic version of the article. A portion is shown here for guidance regarding its form and content.

No.	$S_{1.1\mu m}$ (mJy)	$RA_{1.4}$ (°)	$Dec_{1.4}$ (°)	$S_{1.4}$ (μJy)	Distance (arcsec)	p	RA_{24} (°)	Dec_{24} (°)	S_{24} (μJy)	Distance (arcsec)	p
1	$5.29^{+1.40}_{-1.68}$	...	...	...	...	...	34.411903	−4.559684	95 ± 2	6.7	0.211
2	$3.99^{+1.10}_{-1.34}$	...	...	...	...	...	34.442192	−4.796477	77 ± 7	5.3	0.199
3	$3.75^{+1.22}_{-1.18}$	34.479333	−4.789667	113 ± 20	1.5	0.002	34.479359	−4.789783	776 ± 11	1.3	0.002
4	$4.39^{+1.67}_{-1.58}$	...	...	...	...	...	34.630307	−4.650681	107 ± 5	9.5	0.325
5	$3.57^{+1.19}_{-1.21}$	34.425542	−4.941028	89 ± 17	1.0	0.002	...	...	...	...	0.002
6	$3.99^{+1.27}_{-1.57}$	34.677833	−4.992167	105 ± 16	4.3	0.014	34.677600	−4.991972	924 ± 37	3.7	0.009

SUPPORTING INFORMATION

Additional Supporting Information may be found in the online version of this article:

Table B1. Reliable and tentative radio, 24 μm, 8.0 μm and $i - K$ IDs in the Lockman Hole field.

Table B2. Reliable and tentative radio, 24 μm, 8.0 μm and $i - K$ IDs in the UDS field.

Table B3. All radio and 24 μm IDs in the Lockman Hole field.

Table B4. All radio and 24 μm IDs in the UDS field.

Figure B1. Thumbnail images of AzTEC sources in the Lockman Hole field.

Figure B2. Thumbnail images of AzTEC sources in the UDS field.

Please note: Wiley-Blackwell are not responsible for the content or functionality of any supporting materials supplied by the authors. Any queries (other than missing material) should be directed to the corresponding author for the article.

This paper has been typeset from a TEX/LATEX file prepared by the author.